Materials Today • Volume xxx, Number xx • xxxx 2021 RESEARCH

ELSEVIER

Progress and perspectives on alloying-type anode materials for advanced potassium-ion batteries

RESEARCH: Review

Sumair Imtiaz [1,2], Ibrahim Saana Amiinu [1,2], Yang Xu [3], Tadhg Kennedy [1,2], Chris Blackman [3], Kevin M. Ryan [1,2,*]

[1] Bernal Institute, University of Limerick, Limerick V94 T9PX, Ireland
[2] Department of Chemical Sciences, University of Limerick, Limerick V94 T9PX, Ireland
[3] Department of Chemistry, University College London, 20 Gordon Street, London WC1H 0AJ, UK

Potassium-ion batteries (PIBs) have attracted increasing interest as promising alternatives to lithium-ion batteries (LIBs) for application in large-scale electrical energy storage systems (EESSs) owing to a wide earth-abundance, potential price advantages, and low standard redox potential of potassium. Developmental materials for use in PIBs that can yield high specific capacities and durability are widely sought with emerging studies on alloying-type anode materials offering significant prospects to meet this challenge. Here, recent advances on alloying-type anodes and their composites for PIBs are reviewed in detail and in a systematic way to capture key aspects from fundamental working principles through major progress and achievements to future perspectives and challenges. Emphasis is placed on critical aspects such as the alloying mechanism and correlation of electrode design and structural engineering for performance enhancement and the crucial role of electrolyte compatibility, additives and binders. The review in appraising all the important contributions on this topic allows for a critical assessment of the research challenges and provides insights on future research directions that can accelerate the important development of PIBs as a viable battery energy storage system.

Introduction

Low cost and reliable high energy density EESSs are urgently needed to allow maximum exploitation of renewable electricity generation technologies (e.g., wind and solar power sources) and diminish global dependence on fossil fuels [1–6]. Rocking-chair LIBs have been proven to be an efficient EESS and have dominated advanced portable electronic device and electric vehicle applications due to high energy and power density and long-term cycling stability [7–9]. However, lithium's rarity (only 0.0017 weight (wt.) %), its uneven geographical distribution, and its high cost cannot fulfill the large-scale industrial demands of EESSs [10,11]. Consequently, there is increasing interest in other rechargeable battery technologies such as sodium-ion batteries (SIBs) and PIBs [12,13]. Although sodium is relatively abundant (2.36 wt. %) [14], the standard reduction potential (E^0) of Na^+/Na (−2.71 V vs. standard hydrogen electrode, SHE) is higher than that of Li^+/Li (−3.04 V vs SHE), which strongly limits the energy density of SIBs [15,16].

The high natural abundance of potassium (1.5 wt.%) [10] (Fig. 1a), low cost, fast K^+ transport kinetics in conventional carbonate electrolytes, and comparatively higher energy density than SIBs, arising from the low E^0 of K^+/K (−2.93 V vs SHE) that is very close to that of Li^+/Li, make PIB very attractive. Crucially, the E^0 is even lower than that of Li in some carbonate solvents such as ethylene carbonate (EC): diethyl carbonate (DEC) and propylene carbonate (PC). For example, Komaba et al. [17] experimentally pointed out that the plating/stripping potential of K/K^+ is 0.15 V lower than that of Li/Li^+ in EC:DEC based solvents, making PIBs very promising candidates for EESSs [18–22]. Although, it is obvious that the heavier K will lead to reduced theoretical capacities on a comparative basis, this can be com-

* Corresponding author.
E-mail address: Ryan, K.M. (kevin.m.ryan@ul.ie)

Please cite this article in press as: S. Imtiaz et al., Materials Today, (2021), https://doi.org/10.1016/j.mattod.2021.02.008

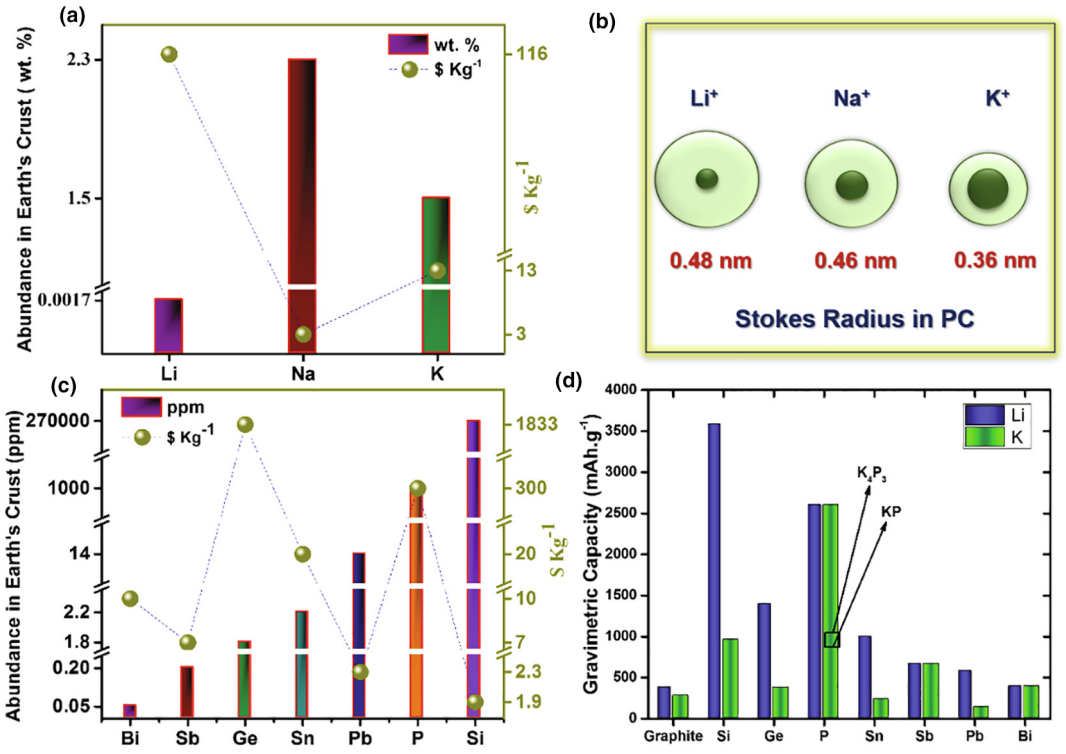

FIGURE 1

(a) Crustal abundance and cost of Li, Na and K. (b) Stokes radii of Li^+, Na^+ and K^+ in PC. (c) Crustal abundance (ppm) and cost of alloying-type anodes (The data for cost of Bi, Sb is taken from Shanghai metals market, Ge from Kitco Metals, Sn and Pb from London metal exchange, P from Chemicool, and Si from Deutsche Rohstoffagentu), and (d) Theoretical specific capacities of anode materials for Li, and K cells (Note: for Si, the formation of K-Si alloy is only demonstrated theoretically. Whereas for P, KP and K_4P_3 are considered the stable alloy and the formation of K_3P is highly speculative, and therefore, they still require more experimental investigations before reliable conclusions can be reached).

pensated by increased energy densities as PIBs produce higher voltages than SIBs and LIBs in several organic electrolytes [21]. Another advantage is that aluminum (Al) foil can be used both as anode and cathode current collector in PIBs, given that potassium does not alloy with Al at lower voltages, leading to significantly reduced weight and price [22–24]. In addition, Al is more stable towards oxidation compared to copper, and thus, can minimize the risk of oxidation of the current collector during over-discharge [22,25]. The ionic radius of potassium (0.138 nm) is larger than lithium (0.068 nm) and sodium (0.097 nm), but because of the weaker Lewis acidity of K^+, its Stoke's radius is smaller (0.36 nm) compared to Li^+ (0.48 nm) and Na^+ (0.46 nm) in PC solvents [26] (Fig. 1b). Furthermore, it has been verified by *ab initio* molecular dynamics (MD) simulations that the diffusion coefficient of K^+ is about three times higher than that of Li^+, signifying that K^+ has better ion-mobility and higher ionic conductivity in K-ion based electrolyte [27]. A challenge for PIBs is that K is highly reactive compared to Na and Li metals. Thermal runaway from a K-ion graphite anode has been reported at lower temperature (100 °C vs. 150 °C-Li) owing to K_xC_8 – electrolyte reactions. However, it does evolve significantly less heat compared to the analogous LIB system (395 J g^{-1} vs. 1048 J g^{-1}) [28]. Furthermore, its much lower melting point (63 °C) is advantageous because it allows for K-dendrites to melt at a safe temperature during overcharging, avoiding internal short circuits and hence leading to enhanced safety in operation [17]. Given these advantages, there is a significant interest in development of high-performance K-based EESSs with high energy density and enhanced rate capability [22,29–31].

Generally, anode materials for rechargeable batteries can be divided mainly into intercalation [32–34], conversion [35,36], organic compounds [37–42] and alloying-type [43–47], based on the relevant reaction mechanism. Intercalation-type anodes mainly include carbon and titanium-based materials which possess intrinsic voids or interlayer spacings to facilitate K^+ transport without significant structural change. While these materials exhibit high cycling stability, the intrinsically limited capacity makes them difficult to attain a high energy density [4]. Among intercalation-type anodes, graphite offers a reasonable reversible capacity of 230 mAh g^{-1}, however, its output voltage is very close to the deposition potential of K, leading to safety issues relating to K metal plating [39,48,49]. Conversion-type anodes, for instance transition metal compounds (M_aX_b, M = Fe, Co, Mn etc.; X = O, S, Se, P, etc.) can provide a high specific capacity, but these materials normally suffer from a large volume change and relative high working potential, leading to unsatisfactory cycle stability and low energy density in a full cell configuration [50,51]. Organic materials are also one of the major class of electrode materials for batteries and are endowed with several advantages over inorganic materials such as low-cost, environmentally friendly characteristics, and structural flexibility for obtaining high electrochemical performance. In addition, the Van der Waals forces between the organic molecules confirm that they provide more free space and lower energy barrier to accommo-

Please cite this article in press as: S. Imtiaz et al., Materials Today, (2021), https://doi.org/10.1016/j.mattod.2021.02.008

date large K-ions [52,53]. However, organic materials have some major issues including dissolution in the electrolyte, poor electronic conductivity, and a relatively low energy density. As an alternative to intercalation, conversion and organic anodes alloying-type anode materials from Group 14 (Si, Ge, Sn and Pb) and Group 15 (P, Sb and Bi) have received increased research attention due to their attractive performances, low working potential, cost-effectiveness (Fig. 1c), and relatively high theoretical capacity which promise high achievable cell energy density [46,54–56]. Fig. 1d compares the gravimetric theoretical capacities of selected anodes for Li and K systems. In general, the electrochemical reactions for alloying-type anode materials can be written as follows:

$$A + xK^{+} + xe^{-} - \leftrightarrow K_xA$$

While the emergence of alloying-type anode materials has been highlighted in previous reviews on PIBs, for instance, Glushenkov's group [57] presented the first comprehensive article in 2018, in which they have summarized the initial development for the anode materials that operate through the alloying–dealloying reaction mechanism. However, the wider scope of these works did not allow for a recent developments of detailed mechanistic insights on the alloying process and the influential factors of nanostructuring, electrolyte composition and binders [48,58,59]. In this review, the working principle of PIBs is discussed followed by the specific reaction mechanisms of the entire range of alloying-type anodes. The approaches for structurally engineering of anodes at the nanoscale for performance enhancement are provided. The importance of electrolyte com-

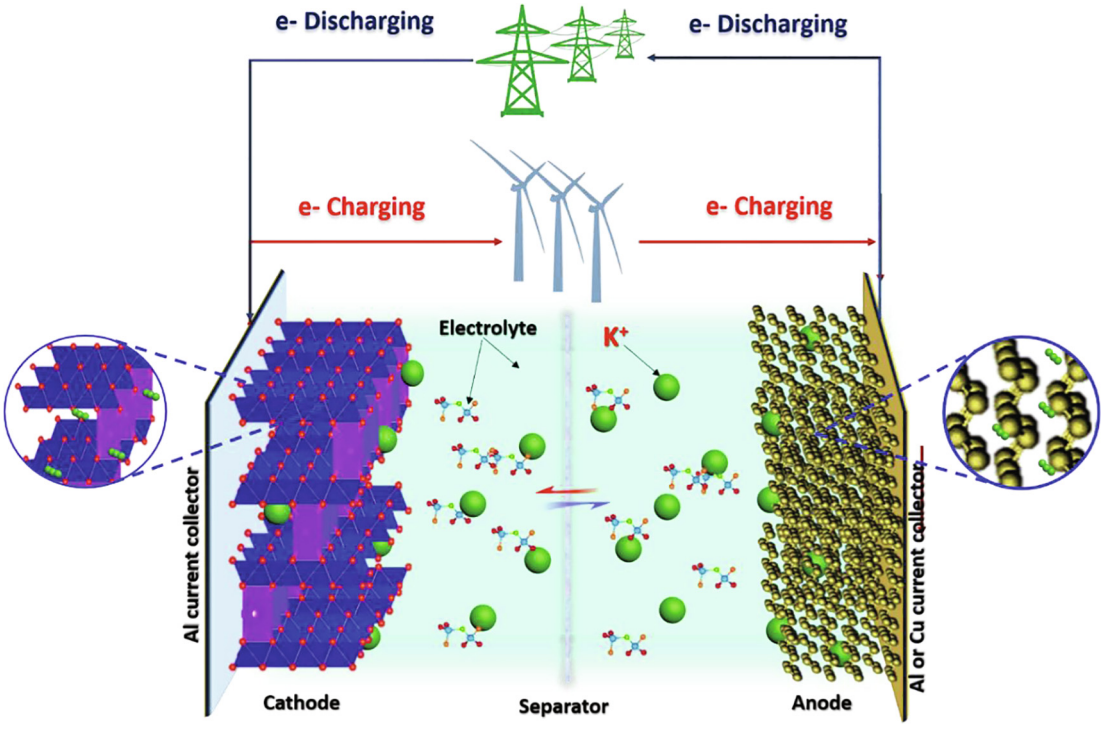

FIGURE 2

Schematic illustration of working principle of "rocking-chair" PIBs based on alloy-type anode (Bi, as an example) and $K_{0.6}CoO_2$ cathode [61].

TABLE 1

Theoretical capacities for the potassiation of group 14 and 15 elements and their estimated percent volume change upon alloying reaction.

Material	Stoichiometry of the final Alloying Product	Theoretical Capacity (mAh g^{-1})	Volume Expansion (%)	Refs.
Si	KSi	954	334	[62]
	$K_{1.1}Si$	1049	unknown	[63]
Ge	KGe	369	unknown	[64]
Sn	KSn	226	~180	[65]
Sb	K_3Sb	660	407	[66]
Bi	K_3Bi	385	>400	[67]
P	K_3P	≤2596	593	[62,68]
	K_4P_3	1154	293	[68]
	KP	865	190	[57,69]
Pb	KPb	126	>259	[70]

Please cite this article in press as: S. Imtiaz et al., Materials Today, (2021), https://doi.org/10.1016/j.mattod.2021.02.008

TABLE 2

Summary of the alloying-type anodes structures and their electrochemical performance for PIBs.

Alloying Anode Type	Anode Material Construction	Synthesis Method	Mass Loading (mg. cm^{-2})	Potential Range (V)	Electrolyte	Capacity Retention (mAh g^{-1})	No. of Cycles	Current Density (mA g^{-1})	Refs.
Sb	Nanoporous Sb	Vacuum distillation	1.5–1.6	0.01–1.2	0.8 M KPF_6 in EC/DEC	318	50	100	[81]
	Sb-C**	Ball milling	3.10	0.05–2.0	1.0 M KPF_6 in PC/EC	650	10	35	[66]
	Sb nanoparticles in 3D carbon	Template assisted freeze drying and carbothermic reduction	1.4–1.8	0.01–2.0	0.8 M KPF_6 in EC/DEC	461	15	200	[75]
	SnSb-graphene-carbon	Electrospinning	~0.85	0.001–2.5	0.8 M KPF_6 in EC/DEC	275.14	100	100	[157]
	Sb@ graphene@carbon	Freeze-drying and heat treatment	1.3–1.7	0.01–3.0	3.0 M KFSI in DME	160	1000	800	[85]
	Sb@3D porous carbon	Liquid-solid absorption mixing method	–	0.001–3.0	1.0 M KPF_6 in EC/DEC	~200	90	100	[83]
	Sb/rGO	Freeze-drying and heat treatment	–	–	1.0 M KPF_6 in PC/EC	331	100	–	[158]
	Sb@RGO	Low-temperature molten salt and Hydrothermal	1.5–2.0	0.05–2.50	0.8 M KPF_6 in EC/PC	210	200	500	[76]
	Sb-NPs@ Porous carbon	Coprecipitation and high temperature annealing	0.6–1.0	0.01–2.6	4.0 M KFSI in EMC	497	100	100	[77]
	Sb@CNF	Electrospinning, ion-exchange and thermal reduction	–	0.01–2.0	2.0 M KFSI in DME	227	1000	1000	[94]
	Ultrafine-Sb@CNFs	Electrospinning and Calcination	~0.8	0.01–3.0	3.0 M KFSI in DME	393	100	200	[78]
	Sb/carbon nanosheets	Solvothermal	~0.8	0.01–2.5	1.0 M KPF_6 in EC/DMC	247	600	200	[84]
	3D porous Sb@carbon	Template method	1.4–1.5	0.01–3.0	5.0 M KFSI in DME	342	260	500	[159]
	Sb-Carbon-rGO	Spraying and pyrolysis	1.0	0.001–1.5	0.8 M KFSI in EC/DEC	245	100	500	[160]
	Sb–graphite	Ball milling and ultrasonication	~1.50	0.01–3.0	– M KFSI in EMC	449.7	100	200	[161]
	Sb nanorod/hollow carbon tube	Hydrothermal and calcination	~1.2	0.01–3.0	1.0 M KFSI in EC/DMC	453.4	80	500	[162]
	Sb@C porous nanofiber	Electrospinning and heat treatment	~1.50	0.01–3.0	1.0 M KFSI in EC/DEC	264	2000	500	[88]
	Sb_2S_3/SNG	Hydrothermal	3.5–4.5	0.1–3.0	1.0 M KPF in EC/DEC	~480	100	50	[97]
	Sb_2Se_3@ N doped Carbon@rGO	Solvothermal, *in-situ* polymerization and calcination	0.6–0.8	0.01–3.0	5.0 M KFSI in EC/DMC	250	350	500	[163]
	Sb_2Se_3 nanodots/carbon	Pyrolysis and co-selenylation	0.8	0.01–2.0	1.0 M KFSI in EC/DEC	312.03	200	1000	[164]
	3D porous Sb-Co nanocomposite	Reduction precipitation	0.8–1.0	0.01–3.0	0.8 M KPF_6 in EC/DEC	402.7	100	60	[165]
Bi	Bi microparticles	Commercial	–	0.1–1.50	1 M KPF_6 in DEGDME	392	100	400	[105]
	Porous network of Bi	Commercial	3.0	0.1–1.50	1.0 M KPF_6 in DME	322.7	300	800	[103]
	Bi@C	Carbothermal reduction	~1.3	0.1–1.50	5.0 M KTFSI in DEGDME	151	35	100	[107]
	Bi@3D porous graphene frameworks	Pyrolysis and self-assembly	1.0	0.2–1.8	1.0 M KPF_6 in DME	164	164	1000	[110]
	Hierarchical Bi nanodots/graphene	Liquid phase exfoliation	~1.0	0.1–2.0	1.0 M KPF_6 in DME	213	500	5000	[166]
	Bi∈NS–C	Gel formation and pyrolysis	0.8–1.0	0.1–1.5	1.0 M KPF_6 in DME	285	1000	5000	[113]
	Bi nanorod@N-doped Carbon	Hydrothermal, polymerization and annealing	–	0.01–1.5	1.0 M KPF_6 in DME	266	1000	3850	[167]
	Bi@C nanorods***	Hydrothermal, polymerization and carbonization	2.11	0.01–3.0	0.8 M KPF_6 in DME	~170	500	1000	[111]

Please cite this article in press as: S. Imtiaz et al., Materials Today, (2021), https://doi.org/10.1016/j.mattod.2021.02.008

TABLE 2 (*CONTINUED*)

Alloying Anode Type	Anode Material Construction	Synthesis Method	Mass Loading (mg. cm^{-2})	Potential Range (V)	Electrolyte	Capacity Retention (mAh g^{-1})	No. of Cycles	Current Density (mA g^{-1})	Refs.
	Ultrathin carbon film@carbon nanorods@Bi nanoparticle	Solvothermal and annealing	0.09–1.30	0.01–3.0	3.0 M KFSI in DME	~327	600	100	[168]
	C@DSBC	Hydrothermal followed by surface coating with polydopamine and calcination	–	0.01–1.5	2.0 M KFSI in DME	~200	100	400	[112]
	Multicore–Shell Bi@N-doped Carbon Nanospheres	Solvothermal and calcination treatment	–	0.1–1.50	1.0 M KPF_6 in DME	203	1000	10,000	[101]
	hollow Bi@N-doped carbon nanorods	Hydrothermal, in-situ reduction and carbonization	1.0–1.2	0.01–1.6	1.0 M KFSI in EC/PC	179.1	300	500	[169]
	Bi nanosheets/rGO membrane**	Sonication, reduction and compression	5.4	0.1–1.5	1.0 M KPF_6 in DME	272	90	500	[170]
	Bismuthene	ultrasonication-assisted electrochemical exfoliation	~1.0	0.01–3.0	1.0 M KPF_6 in DME	200	2500	20,000	[171]
	BiOCl nanoflakes	Solvothermal method	1.0–2.0	0.01–2.0	1.0 M KFSI in EC/DEC	213	50	50	[172]
	Bi_2MoO_6 microsphere	Solvothermal method	~1.2	0.01–3.0	3.0 M KFSI in DME	121.7	600	100	[173]
	CuBi Binary Alloy	Chemical dealloying process	0.8–1.0	0.01–2.0	1.0 M KFSI in DME	270	50	50	[108]
	$Bi_{0.51}Sb_{0.49}OCl$/rGO	Ultrasonication, followed by reduction and freeze-drying process	~1.0	0.01–2.70	3.0 M KFSI in DME	360	1000	100	[174]
	Bi_xSb_{1-x}@P	Solution precipitation method	~0.8	0.05–2.0	4.0 M KFSI in DME	295.4	800	500	[114]
	SbBi@C	Freeze-drying and pyrolysis	~1.0	0.02–2.5	5.0 M KFSI in DME	320	600	500	[117]
	$(Sb,Bi)_2S_3$ nanotubes	coprecipitation method	~1.0	0.01–2.2	3.0 M KFSI in DME	353	1000	500	[118]
Sn	Sn-C	Ball-milling	1.3	0.01–2.0	0.75 M KPF_6 in EC/DEC	110	30	25	[124]
	Sn submicron-particles@RGO	Freeze-drying and thermal reduction	~1.0	0.01–3.0	0.8 M KPF_6 in EC/DEC	200	50	100	[128]
	3D hierarchically porous carbon/Sn	Mixing, gel-like precipitation and calcination	–	0.01–3.0	0.8 M $KClO_4$ in EC/DEC	276.4	100	50	[126]
	Sn/N-doped porous carbon	Sol-gel method and heat treatment	–	0.01–2.6	1.0 M KPF_6 in EC/DEC	198	200	50	[127]
	SnO	Precipitation method	~0.8	0.005–2.0	0.5 M KPF_6 in EC/DEC	183	30	25	[129]
	SnO_2@Stainless Steel Mesh	Hydrothermal	1.6	0.01–2.6	1.0 M KPF_6 in EC/DEC	351	100	50	[175]
	SnO_2@Carbon Foam	Electro-deposition method	–	0.01–3.0	0.8 M KPF_6 in EC/DEC	231.7	400	1000	[176]
	SnO_2-graphene-carbon nanofibers	Electrospinning method	~0.85	0.00–2.5	0.8 M KPF_6 in EC/DEC	202.06	100	100	[177]
	Phosphoric acid doped SnO_2–graphene–carbon nanofibers	Electrospinning method	~0.85	0.001–2.5	0.8 M KPF_6 in EC/DEC	285.9	60	100	[178]
	3D SnO_2@C	Freeze-drying followed with sintering and dealloying strategy	0.8–1.0	0.01–3.0	0.8 M KPF_6 in EC/DEC	270.3	200	100	[179]
	Sandwich-like MoS_2@SnO_2@C nanosheets	Hydrothermal reactions	0.8–1.0	0.01–3.0	0.8 M KPF_6 in EC/DEC	312	25	50	[180]
	SnS_2/SnO_2	Two-step hydrothermal method	1.0	–	1.0 M KPF_6 in EC/DEC	155	250	500	[181]

(continued on next page)

Please cite this article in press as: S. Imtiaz et al., Materials Today, (2021), https://doi.org/10.1016/j.mattod.2021.02.008

TABLE 2 (*CONTINUED*)

Alloying Anode Type	Anode Material Construction	Synthesis Method	Mass Loading (mg. cm^{-2})	Potential Range (V)	Electrolyte	Capacity Retention (mAh g^{-1})	No. of Cycles	Current Density (mA g^{-1})	Refs.
	SnS_2–rGO***	Sulfidization of GO supported peroxostannate and heat treatment	0.8–0.93	0.01–2.0	0.75 M KPF_6 in EC/DEC	~ 250	30	25	[182]
	SnS_2/Graphene**	Hydrothermal process followed by freeze drying	–	0.01–2.5	0.8 M KPF_6 in EC/DEC	559	50	100	[183]
	SnS_2@rGO	Solvothermal method	1.0–2.0	0.01–2.0	0.8 M KPF_6 in EC/DEC	205	300	1000	[184]
	SnS_2@C@rGO	Calcination of disodium stannous citrate, followed by GO coating and sulfuration	–	0.01–3.0	0.8 M KFSI in EC/DEC	309	100	100	[185]
	SnS_2/N-Doped Graphene	Hydrothermal method	0.8–1.2	0.01–3.0	1.0 M KFSI in EC/DEC	335	200	1000	[186]
	N, S-doped Carbon/SnS_2 nanosheet	In-situ carbonization and sulfuration method	~1.0	0.01–3.0	1.0 M KFSI in EC/DEC	502.7	50	100	[187]
	SnSb	Ball milling	2.0–2.5	0.00–2.0	0.8 M KFSI in EC/DEC	282	40	0.2*	[115]
	3D SnSb@N-doped Carbon	NaCl-template assisted *in-situ* pyrolysis strategy	~1.0	0.01–2.2	0.5 M KPF_6 in DME	185.8	200	500	[130]
			~1.0	0.01–2.2	0.8 M KPF_6 in EC/DEC	147.4	200	500	[130]
	NiSn@C	Colloidal route and sonication	–	0.01–3.0	3 M KTFSI in DME	167	400	200	[131]
	CoSn@C	Colloidal route and sonication	–	0.01–3.0	3 M KTFSI in DME	84	300	200	[131]
P	BP–C	Ball milling	1.1–1.5	0.01–2.0	0.75 M KPF_6 in EC/DEC	270	50	50	[69]
	P/Activated carbon	Vaporization-condensation-conversion approach	1.0–1.5	0.01–3.0	0.5 M KPF_6 in EC/PC	~90	50	500	[188]
	P/Carbon nanotube-backboned mesoporous carbon	Vaporization-condensation-conversion approach	0.8–1.0	0.01–2.0	0.6 M KPF_6 in EC/PC	244	200	500	[189]
	RP@rGO	Vaporization-condensation method	0.9–1.2	0.001–3.0	0.8 M KPF_6 in EC/DEC	253	500	500	[190]
	Red P/C	Ball milling	–	0.001–3.0	0.8 M KPF_6 in EC/DEC	71.5	500	500	[135]
	Red P@Carbon nanosheet**	Carbonization followed by Vaporization-condensation	~0.7	0.01–2.0	0.8 M KPF_6 in EC/DEC	427.4	40	100	[139]
	Red P/C**	Wet ball milling	0.75–1.10	0.01–2.5	1.0 M KTFSI in EC/DEC	~300	60	1000	[191]
	red P@N-PHCNFs	Electrospinning, carbonization and vaporization-condensation	~1.0	0.01–2.0	0.7 M KPF_6 in EC/DEC	465	800	2000	[141]
	PPy coated P@activated carbon	Vaporization-deposition-conversion followed by polymerization	1.0–1.2	0.01–2.0	1.0 M KFSI in EC/DEC	220	100	500	[192]
	Black P–Graphite**	Low-pressure transport route and ball milling	1.2	0.01–2.0	- M KPF_6 in EC/DEC	600	50	250	[193]
	Red P/MoS_2	Ball milling	–	0.01–2.0	0.8 M KPF_6 in EC/DEC	118	500	1000	
	Sb–P–C	Magneto-ball milling	1.1–1.5	0.01–2.0	0.75 M KPF_6 in EC/DEC	402	50	50	[79]
	Sn_4P_3/rGO	Ball milling	~1.2	0.05–2.8	0.8 M KPF_6 in EC/DEC	157.3	60	600	[147]
	$SnP_{0.94}$@GO	Hot-injection colloidal method followed by ultrasonication and mixing	~0.42	0.01–2.0	1.0 M KFSI in EC/DEC	106	100	200	[148]
	Sn_4P_3/C**	Ball milling	~0.78	0.01–2.0	0.8 M KPF_6 in EC/DEC	307.2	50	50	[134]

Please cite this article in press as: S. Imtiaz et al., Materials Today, (2021), https://doi.org/10.1016/j.mattod.2021.02.008

TABLE 2 (*CONTINUED*)

Alloying Anode Type	Anode Material Construction	Synthesis Method	Mass Loading (mg. cm^{-2})	Potential Range (V)	Electrolyte	Capacity Retention (mAh g^{-1})	No. of Cycles	Current Density (mA g^{-1})	Refs.
	Sn_4P_3@Carbon fibers**	Ball milling and electrospinning method	–	0.01–2.0	1.0 M KFSI in EC/DEC	403.1	200	50	[149]
	FeP/C	Ball milling	–	0.01–3.0	0.8 M KPF_6 in EC/DEC	~182	50	50	[194]
	N-doped hollow carbon nanofibers @FeP	Hydrothermal and phosphidation treatment	~1.0	0.005–3.0	0.8 M KClO4 in EC/DEC	210	1000	100	[195]
	FeP@foam-like graphenic scaffolds	Pyrolysis-blowing method, followed by phosphorization treatment	~1.0	0.01–3.0	1.0 M KFSI in DME	183	1000	3000	[196]
	Ni-Fe-P/N-doped carbon nanoboxes	Epitaxial deposition and phosphorization	1.0–1.2	0.01–3.0	3.0 M KFSI in TEGDME	172.9	1600	500	[197]
	MoP@N, P codoped carbon nanofibers	Electrospinning method combined with carbonization and phosphorization	–	0.01–3.0	0.8 M KPF_6 in EC/DEC	280	200	100	[198]
	Se_3P_4@mesoporous carbon**	Ball milling and heat treatment	~1.0	0.01–3.0	0.8 M KPF_6 in EC/DEC + FEC	~380	300	1000	[199]
	SeP/C	Plasma-assisted ball milling	–	0.01–3.0	1.0 M KFSI in DME	248.6	120	1000	[200]
	GeP_5	Ball milling	–	0.01–3.0	1.0 M KFSI in EC/DEC	213.7	2000	500	[154]
Ge	Nanoporous Ge	Chemical-dealloying method	1.0–1.5	0.01–2.5	0.5 M KPF_6 in EC/DEC	120	400	20	[64]
	Germanane	Topotactic chemical deintercalation	–	0.0–2.0	0.8 M KFSI in EC/DEC	150	30	0.05*	[155]
Pb	Pb	Commercial	2.0–2.5	0.0–0.8	0.8 M KFSI in EC/DEC	75	20	0.2*	[70]

*Current density based on C-rate.
**Capacity based on the mass of alloying/conversion active material.
*** Capacity based on the total mass of the electrode (including active material (Alloying + Matrix), binder and carbon additive).
All remaining capacity data presented here is based on the mass of composite (Alloying material + Matrix or Alloying/Conversion material + Matrix).

patibility, salt chemistry and binders for alloying-type anodes is further described. Lastly, insights are offered into the challenges and opportunities for future development of PIBs.

Working principle of PIBs

PIBs use a similar "rocking-chair" working principle to that of LIBs, in which K^+ shuttle between the anode and cathode via either a non-aqueous or an aqueous K^+ electrolyte during the charge/discharge process [16,60]. A schematic of the components in an alloying anode based PIB and its operation is illustrated in Fig. 2. Electrical energy is stored/released through a redox reaction at the anode and cathode side. The cathode and anodes are coupled through a separator, immersed in electrolyte. The purpose of the separator is to provide appropriate transport of ionic charge between electrodes and avoid short circuit. During the charging process, the cathode is oxidized to release K^+ and electrons that subsequently reach the anode through the electrode and an external circuit, respectively. Upon reaching the anode side, a reduction process occurs leading to electron acquisition and K^+ insertion. The reverse process occurs during discharge, in which K^+ and electrons flow from the anode to the cathode [29]. Alloying-type anodes have recently been studied in PIBs because they provide higher capacities than carbonaceous materials, yet the large volume expansion (Table 1) and sluggish reaction kinetics are the major challenges that needs to be addressed. Numerous efforts have been devoted so far to overcome those issues including nanostructuring of the electrode, combination of the alloying element with a carbonaceous matrix, and judicious selection of binders, additives and solvents to the electrolyte. Table 2 collates the reports of alloying-type anode materials and their electrochemical performance in PIBs with a detailed discussion according to alloying element, and electrolyte system outlined in the coming sections.

Alloy-type materials for potassium-ion battery

Sb-based anodes

Antimony (Sb) is one of the most considered alloying anode materials for PIBs, because of its high electrical conductivity (2.56×10^6 S m^{-1}), low potassiation potential and high theoretical capacity [71,72]. Sangster et al. [73] reported the binary K-Sb system in 1993, based on thermodynamically stable K–Sb alloy phases. According to the K-Sb binary phase diagram, there exists four intermediate phases transitioning from KSb_2 to KSb, K_5Sb_4 and then K_3Sb with the theoretical capacities of 110, 220, 275, and 660 mAh g^{-1}, respectively [73,74]. Fig. 3a shows the structural evolution from Sb to K_3Sb during the potassiation process

Please cite this article in press as: S. Imtiaz et al., Materials Today, (2021), https://doi.org/10.1016/j.mattod.2021.02.008

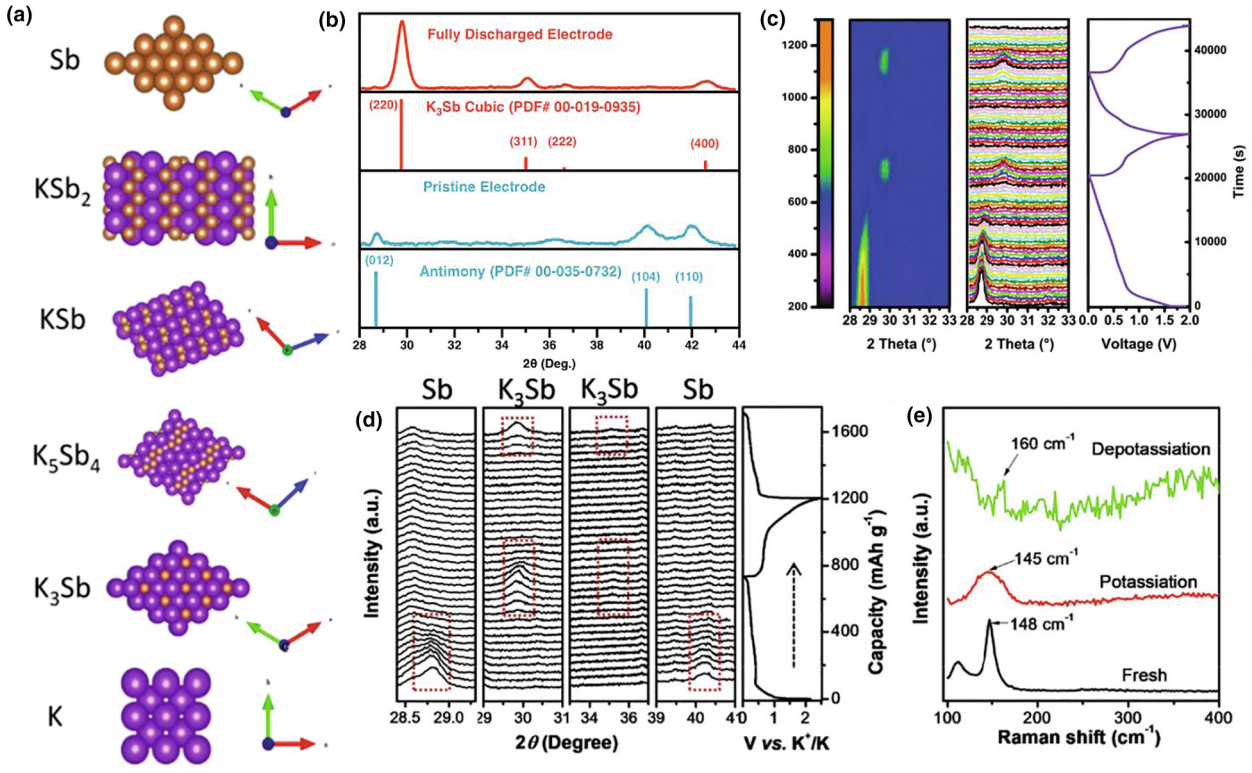

FIGURE 3

(a) Crystal structure of K and stages of the structure evolution from Sb to K_3Sb during the potassiation process Reproduced with permission [74], © Royal Society of Chemistry, 2019 (b) XRD patterns of a pristine and fully discharged Sb/C electrode. Reproduced with permission [66]. © American Chemical Society, 2015 (c) *In-situ* XRD patterns of the Sb based electrode during the galvanostatic depotassiation/potassiation process at 100 mA g^{-1}. Reproduced with permission [75], © Royal Society of Chemistry, 2018 (d) *In-situ* XRD patterns and (e) *Ex-situ* Raman spectra obtained by testing the fresh, fully potassiated and depotassiated of Sb nanoparticles, respectively. Reproduced with permission [76], © Royal Society of Chemistry, 2018.

[74]. The first study of Sb as an anode in PIBs was reported by McCulloch et al. in 2015 [66]. A mixture of bulk Sb powders and carbon black was milled in a planetary ball mill, and the obtained Sb/C sample was tested in a half-cell using 1.0 M potassium hexafluorophosphate (KPF_6) in PC/EC 1:1 (w/w) electrolyte. Cyclic voltammetry (CV) suggested a two-step discharge process, and the Sb/C anode delivered a reversible capacity of 650 mAh g_{Sb}^{-1}. Based on the obtained capacity, K_3Sb was proposed as the final alloy phase, which was verified by *ex-situ* X-ray diffraction (XRD) of the fully discharged anode (Fig. 3b). Mai's Group [75] further studied the electrochemical alloying mechanism by *in-situ* XRD (Fig. 3c). They observed a two-step alloying process for Sb. First, the crystalline Sb gradually transformed into an intermediate amorphous phase K_xSb ($0 < x < 3$), and then, crystallized to cubic K_3Sb. Upon charging, the diffraction peak intensities of the K_3Sb gradually decreased accompanied by the emergence of the intermediate phase of K_xSb. With further charging, the intermediate phase of K_xSb gradually transformed into amorphous Sb. Yi et al. [76] also explored the potassiation/depotassiation process of the Sb nanoparticles by *in-situ* XRD and ex-situ Raman spectra (Fig. 3d and e). During the potassiation process, the characteristic peaks of hexagonal Sb decreased gradually, while the characteristic peaks of the cubic K_3Sb phase emerged. It is noteworthy that after fully depotassiation, the characteristic peaks of the cubic K_3Sb phase completely vanished, but no characteristic peaks of Sb were detected, which indicated that amorphous Sb was obtained after potassium was extracted from the K_3Sb phase. During the second potassiation process, the characteristic peaks of the cubic K_3Sb phase appeared again with high intensity. This suggested that the amorphous Sb fully transformed to the cubic K_3Sb phase in subsequent cycles. These in-situ XRD results confirmed the formation of a cubic K_3Sb phase when fully potassiated and an amorphous phase when fully depotassiated. Furthermore, ex-situ Raman spectroscopy also verified the results obtained by in-situ XRD. As shown in Fig. 3e, the fresh electrode exhibited a Raman peak at 148 cm^{-1}, which changed to a broad peak at 145 cm^{-1} after full potassiation, indicating the formation of cubic K_3Sb phase. Moreover, after the depotassiation process, this peak was replaced by a weak one at 160 cm^{-1}, further suggesting the formation of amorphous Sb. Using *operando* XRD measurements, Monconduit and co-workers [67] confirmed the formation of the cubic K_3Sb although they also noted a small contribution of the hexagonal K_3Sb. The alloying mechanism of Sb can be summarized as [75].

$$Sb + xK^+ + xe^- \leftrightarrow K_xSb \quad (1)$$

$$K_xSb + (3-x)K^+ + 3 - -xe^- \leftrightarrow K_3Sb \quad (2)$$

Whilst Sb is one of the most promising alloy anode materials, extensive volume expansion (~407%) [67] during the potassium alloying reaction causes fracture of the active material and its delamination from the current collector resulting in rapid capacity fade [77–79]. Several strategies have been proposed to accommodate the volume expansion and enhance the electrochemical

Please cite this article in press as: S. Imtiaz et al., Materials Today, (2021), https://doi.org/10.1016/j.mattod.2021.02.008

performance of Sb-based anode materials. Sb-based anode materials with porous structures have been considered due to the ability to accommodate large volume changes during the alloying-dealloying process arising from the void and holes [80]. An et al. [81] designed a three-dimensional (3D) nanoporous antimony (NP-Sb) with tunable morphology and porosity from a commercial Zn-Sb alloy *via* a physical vacuum-distillation method. Fig. 4a and b compare the cycling capability and rate capability of NP-Sb and bulk Sb respectively. NP-Sb showed improved cycling stability, achieving 510 mAh g^{-1} capacity in the 2nd cycle and 318 mAh g^{-1} after 50 cycles, whereas the bulk Sb retained only 19 mAh g^{-1} after 50 cycles. In addition, the rate performance of NP-Sb was consistently improved compared to the bulk-Sb counterpart. A schematic of the potassiation process for bulk-Sb and NP-Sb is illustrated in Fig. 4c and d. The improved electrochemical performance of NP-Sb is attributed to the 3D porous structure with interconnected ligaments, which can buffer the large volume expansion and accelerate the K^+ transport during the redox reaction. Another promising strategy to address the volume issue is to obtain an Sb-based carbon composite [78,82–85]. For example, Mai's group [75] confined Sb nanoparticles in a 3D carbon framework (denoted as 3D SbNPs@C) via a template-assisted freeze-drying treatment and subsequent carbothermic reduction. Scanning electron microscopy (SEM) and transmission electron microscopy (TEM) images confirmed that the as-synthesized 3D SbNPs@C had a well-interconnected 3D carbon framework on which numerous antimony nanoparticles in the range of 60–100 nm were anchored, forming a honeycomb-like structure (Fig. 4e and f). The structural design of 3D SbNPs@C is shown in Fig. 4g, and combines both a 3D network and a high capacity of Sb. The authors suggested that this 3D structure increased the effective contact area between the electrode and electrolyte, thereby buffering the volume changes and greatly enhancing the conductivity and effectively suppressed the agglomeration of Sb particles. As an anode in PIBs, 3D SbNPs@C exhibited a high reversible capacity of ~478 mAh g^{-1} at 200 mA g^{-1} and rate capacity of ~288 mAh g^{-1} at the high current density of 1000 mA g^{-1}. Yi et al. [76] coated Sb nanoparticles with reduced graphene oxide (Sb@RGO) and studied the electrochemical performance against Sb nanoparticles and bulk Sb. The monodispersed Sb nanoparticles were first synthesized with a size of ~55 nm *via* the reduction of $SbCl_3$ by metallic Al in the molten salt of $SbCl_3$ at 80 °C, and the Sb@RGO composite was obtained by a hydrothermal synthesis and calcination processes. The results showed that coating with RGO provided more stable cycling capacity and rate capability. Sb@RGO delivered a stable capacity of about 300 mAh g^{-1} at a current density of 200 mA g^{-1} after 40 repeated cycles. In addition, at the current densities of 100, 300 and 1000 mA g^{-1}, the composite showed reversible capacities of 381, 317 and 222 mAh g^{-1}, respectively. Even at 2000 and 5000 mA g^{-1} after 40 and 50 cycles, the capacity was retained at 172 and 100 mAh g^{-1}, corresponding to a capacity retention ratio of 45.1 and 26.3%, respectively. These results were attributed to the monodispersed Sb nanoparticles and graphene coating which provided plenty of active sites for K^+ storage and transportation.

Although, these electrode configurations with Sb and carbon delivered high reversible capability and long cycling stability, they were assembled by adhering active materials to the current collector with inactive binders, which reduces the overall energy density of the battery. In contrast, an integrated electrode design without the inactive binders can provide long cycling stability and excellent rate capability [86,87]. In this regard, a flexible integrated electrode was constructed by confining Sb nanoparticles (about 4 nm) in interconnecting carbon porous nanofibers (Sb@C PNFs) using a scalable electrospun assisted deposition strategy [88]. Electrospinning of a solution containing poly (methyl methacrylate) (PMMA), polyacrylonitrile (PAN), and $SbCl_3$ in *N*,*N*-dimethylformamide (DMF), followed by annealing in an argon (Ar) atmosphere gave Sb@C PNFs. Fig. 4h and 4i show the digital images of the Sb@C PNFs precursor and Sb@C PNFs twisted around a pencil, showing the flexibility of the electrode. A 3D continuous porous conductive framework was observed by SEM (Fig. 4j) and TEM (Fig. 4k), which indicated that the carbon porous nanofibers contained vessel-like channels (similar to the vessels in plants). The unique structure was due to the decomposition of PMMA, which is beneficial to create pores and channels among CNFs. The as-prepared flexible Sb@C PNFs integrated electrode was evaluated in PIBs with 1 M potassium bis(fluorosulfonyl)imide (KFSI) in EC:DEC (1:1 in volume), exhibiting reversible capacities of 399, 310, and 208 mAh g^{-1} at 0.1, 2, and 5 A g^{-1}, respectively. Even after 500 cycles, a capacity of 264 mAh g^{-1} was obtained at 2 A g^{-1} (Fig. 4l). The solid electrochemical performance of Sb@C PNFs was ascribed to the vessel-like channels which provided accessibility for the electrolyte to reach the Sb nanoparticles, shortened K^+ diffusion distances due to the ultra-small Sb nanoparticles, and reserved space to adapt the volume swelling during cycling. In addition, XRD, TEM, and *in-situ* Raman analysis confirmed the highly reversible alloying/dealloying process between cubic K_3Sb and as-formed amorphous Sb. Recently, advanced *operando* characterization techniques such as *in-situ* (TEM, XRD, Raman etc.) have provided more insights into materials design and has led to better structural design of electrode materials for LIBs and SIBs [89–93]. Considering the large volume change of alloying materials after potassiation compared to lithiation and sodiation, these studies are of high importance in PIBs to guide the structural design of alloying anodes. Huang et al. [94] employed *in-situ* TEM to reveal the insights of the structural changes during potassiation of Sb. A binder-free hybrid structure with Sb nanoparticles as the yolk confined in carbon shell (Sb@C) embedded in carbon nanofibers (Sb@CNFs) was prepared by electrospinning, ion-exchange and thermal reduction (Fig. 4m). For *in-situ* TEM observations, a nano PIB was fabricated with K metal and as prepared Sb@CNFs, in which a K_2O layer on the surface of K-metal acted as a solid electrolyte (Fig. 4n). It can be seen in Fig. 4o that K^+ inserted into the carbon fiber and then infiltrated into the Sb@C nanobox. The Sb nanoparticles slowly become larger and almost filled the interior void space of the carbon shell after discharging for 60 min. Importantly, the volume expansion of Sb nanoparticles and carbon shells was about 404% and 220%, respectively, which confirmed that the internal void space in the carbon shell could relieve the overall volumetric expansion of Sb-based material during the potassiation process. During the depotassiation process, the volume of the Sb@C nanobox shrank gradually, but did not recover to the initial state (Fig. 4p), reveal-

Please cite this article in press as: S. Imtiaz et al., Materials Today, (2021), https://doi.org/10.1016/j.mattod.2021.02.008

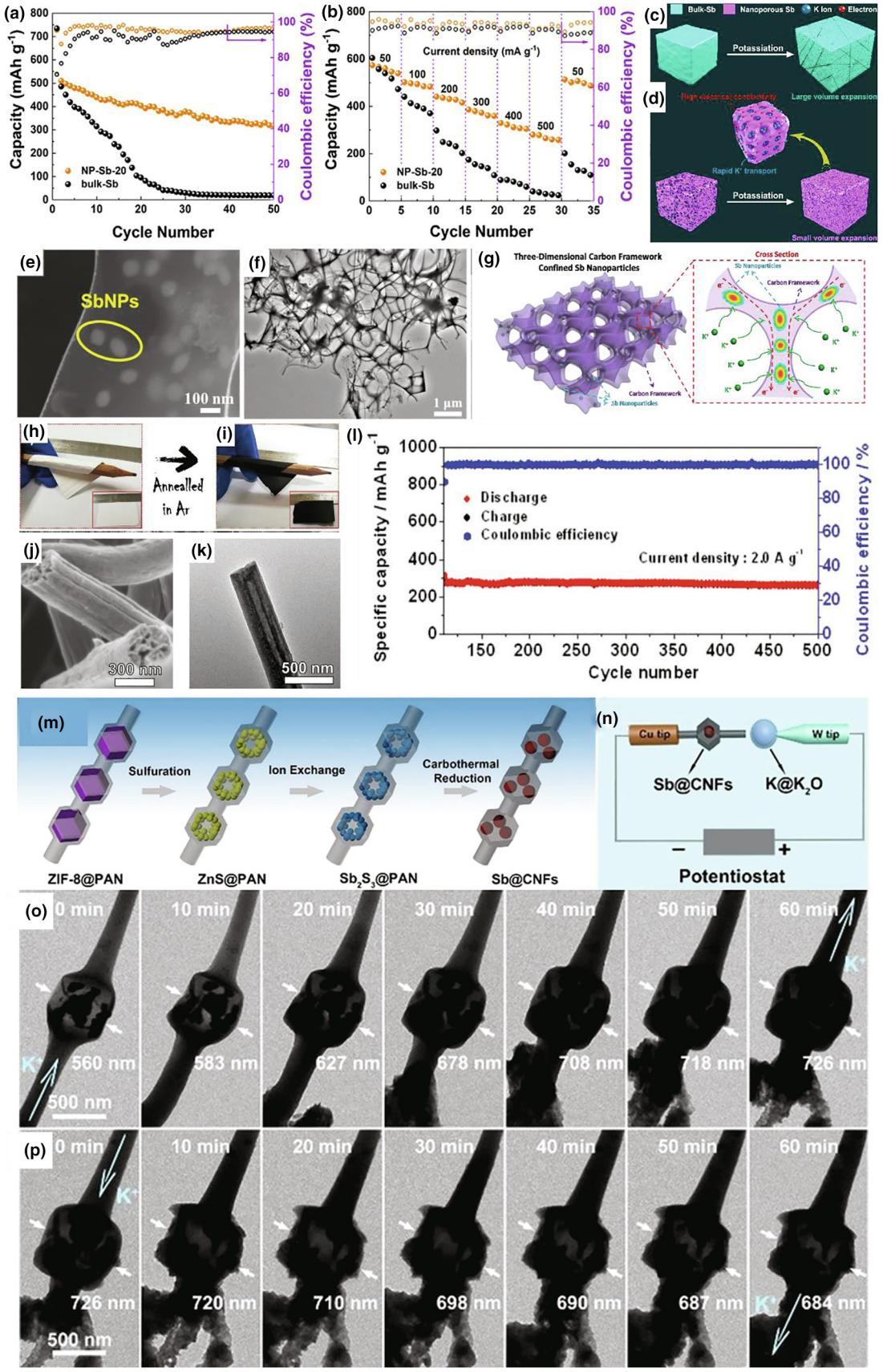

Please cite this article in press as: S. Imtiaz et al., Materials Today, (2021), https://doi.org/10.1016/j.mattod.2021.02.008

ing that K^+ failed to completely extract from CNFs and Sb. Notably, this real-time observation showed that after repeated K^+ insertion/extraction processes, the overall structure of Sb@CNF remained stable without pulverization. As a result it displayed superior rate performance and afforded a capacity of 227 mA h g^{-1} at 1000 mA g^{-1} after 1000 cycles.

Metal sulfides (M_xS_y) are another important material for anodes, that can follow the conversion and conversion/alloying-coupling type reaction depending on whether M is electrochemically active or inactive. Generally, conversion/alloying-coupling type metal sulfides exhibit higher specific capacities than their individual conversion-type counterparts, but again the volume expansion is an issue, and hence optimization of the capacity and structural integrity is an important prerequisite for application in PIBs [36,95,96]. Considering these factors, Chen et al. [97] designed an antimony sulfide (Sb_2S_3) and graphene composite (Sb_2S_3/SNG) as a self-supported anode consisting of Sb_2S_3 nanoparticles (~20 nm) and S, N-codoped graphene by a facile hydrothermal co-assembly approach. This Sb_2S_3/SNG composite delivered a reversible capacity of 537 mAh g^{-1} at 50 mA g^{-1}, with a good cycling stability of 89.4% over 100 cycles. The stable performance was attributed to the porous co-doped graphene framework, which provided structural integrity and alleviated volume expansion stress. Besides, Guo's group [98] explored a few-layered antimony sulfide/carbon sheet (Sb_2S_3/C) anode for PIBs, which delivered a reversible capacity of 404 mAh g^{-1} after 200 cycles at a current density of 500 mA g^{-1}. Latterly, the reaction mechanism and electrochemistry of Sb_2S_3–rGO composite for PIBs was analyzed by Glushenkov and co-workers [99]. The Sb_2S_3–rGO composite anode was synthesized by the peroxide route and its behavior was observed experimentally in different electrolyte formations. These results demonstrated that the Sb_2S_3–rGO anode can provide depotassiation capacities in excess of 650 mAh g^{-1}, which was superior to other reported Sb_2S_3 containing electrode materials [97,98,100]. The reaction mechanism in the Sb_2S_3 phase was observed by post cycling XRD analysis and *in-situ* TEM, which revealed that it involved alloying-conversion processes with alloy phases such as K_3Sb and potassium polysulphides such as K_2S_3. The general equation for this reaction can be written as ($Sb_2S_3 + xK^+ + xe^- \leftrightarrow yK_3Sb + zK_2S_3$), which was similar to the other reports [97,98]. However, the authors proposed that the charge storage mechanism for the Sb_2S_3 phase involves more than eight electrons per formula unit, as a result higher capacity is possible in Sb_2S_3-based anodes. In addition, an interesting fact was highlighted for the co-existance of alloying and conversion reaction process of Sb_2S_3 in a more complicated manner then simplistically represented in the literature as two sequential reactions of conversion and alloying for LIBs and SIBs. Nevertheless, although a high capacity can be obtained from these Sb-based anodes, the reaction processes of these anodes needs to be properly identified in order to extract their full potential in PIBs.

Bi-based anodes

The Group 15 element bismuth (Bi) is less popular as an alloying anode in LIBs, probably due to the low gravimetric capacity compared to Si, Ge and Sn. However, the reported results suggest that it could stand out as the most attractive candidate for K-ion insertion owing to its large crystal lattice along the *c*-axis (0.395 nm), low average potential, relatively flat plateaus and ability to alloy with three potassium ions to form a stable K_3Bi phase, providing a theoretical capacity of 385 mAh g^{-1} [59,101–103]. K–Bi liquid alloys were studied as far back as 1988 [104], but the room temperature phase transition has remained largely unexplored. Huang et al. [105] revealed the alloying mechanism of Bi in PIBs by *in-situ* XRD of Bi microparticles as the anode, in conjunction with density functional theory (DFT) analysis. Fig. 5a shows the galvanostatic charge/discharge of a Bi microparticle anode where only a single long plateau at 0.4 V was detected in the initial alloying process; whereas three plateaus were detected in the subsequent dealloying/alloying processes delivering a reversible capacity of 400 mAh g^{-1}. Fig. 5b shows the phase transition of the Bi electrode by *in-situ* XRD measurements where cubic KBi_2 and monoclinic K_3Bi_2 were observed when 0.5 moles of potassium were consumed (Fig. 5b, red line). In the subsequent potassiation, hexagonal-phase K_3Bi emerged and rapidly grew in concentration with the disappearance of K_3Bi_2, while KBi_2 reached a certain intensity and then remained almost constant. The coexistence of KBi_2 and K_3Bi, and their intensity variations along the plateau, suggested a surface potassiation route, where KBi_2 served as the reaction frontier (Fig. 5c). At the end of the discharge, K_3Bi became the final phase at the expense of KBi_2 and any unreacted Bi. Fig. 5d summarizes the alloying and dealloying processes in the Bi electrode after the first discharge, illustrating that the reversible dealloying/alloying follows the stepwise K_3Bi–K_3Bi_2–KBi_2–Bi mechanism in the following cycles. In a related study, Zhang et al. [106] proposed the formation of a Bi (K) solid solution followed by K_5Bi_4 and K_3Bi, whilst a two-step process from Bi to KBi and K_3Bi was indicated *via ex-situ* XRD by Sun and co-workers [107]. However, in studies carried out under *operando* conditions [67] and using Rietveld refinement of the *ex-situ* XRD pattern [103], KBi and K_5Bi_4 phases were not detected in agreement with the formation of three phases as suggested by Huang et al. [105]. In a very recent study supported by

FIGURE 4

(a) Cycling performance of NP-Sb and bulk-Sb anodes at 100 mA g^{-1}, (b) Rate capability of bulk-Sb and NP-Sb at 50 to 500 mA g^{-1}. (c, d) Schematic of the potassiation process for bulk-Sb and NP-Sb, respectively. Reproduced with permission [81] © American Chemical Society, 2018. (e) SEM and (f) TEM images of 3D SbNPs@C, (g) Schematic illustration of the 3D SbNPs@C hybrid electrode with large electrode–electrolyte contact area, fast electron transport network, and short K-ion diffusion distances. Reproduced with permission [75], © Royal Society of Chemistry, 2018. Digital photos of the (h) Sb@C PNFs precursor and (i) Sb@C PNFs twisted around a pencil and in the plane (the inset of (h) and (i), (j) SEM and (k) TEM images of the as-prepared Sb@C PNFs. (l) Cycling performance of Sb@C PNFs at 2.0 A g^{-1} Reproduced with permission [88] © Wiley-VCH. 2020. Illustration of the (m) synthesis process for Sb@CNFs and (n) *in-situ* TEM device, Time-lapse TEM images of single Sb@CNF during (o) first potassiation and (p) first depotassiation. Reproduced with permission [94] © Wiley-VCH. 2020.

Please cite this article in press as: S. Imtiaz et al., Materials Today, (2021), https://doi.org/10.1016/j.mattod.2021.02.008

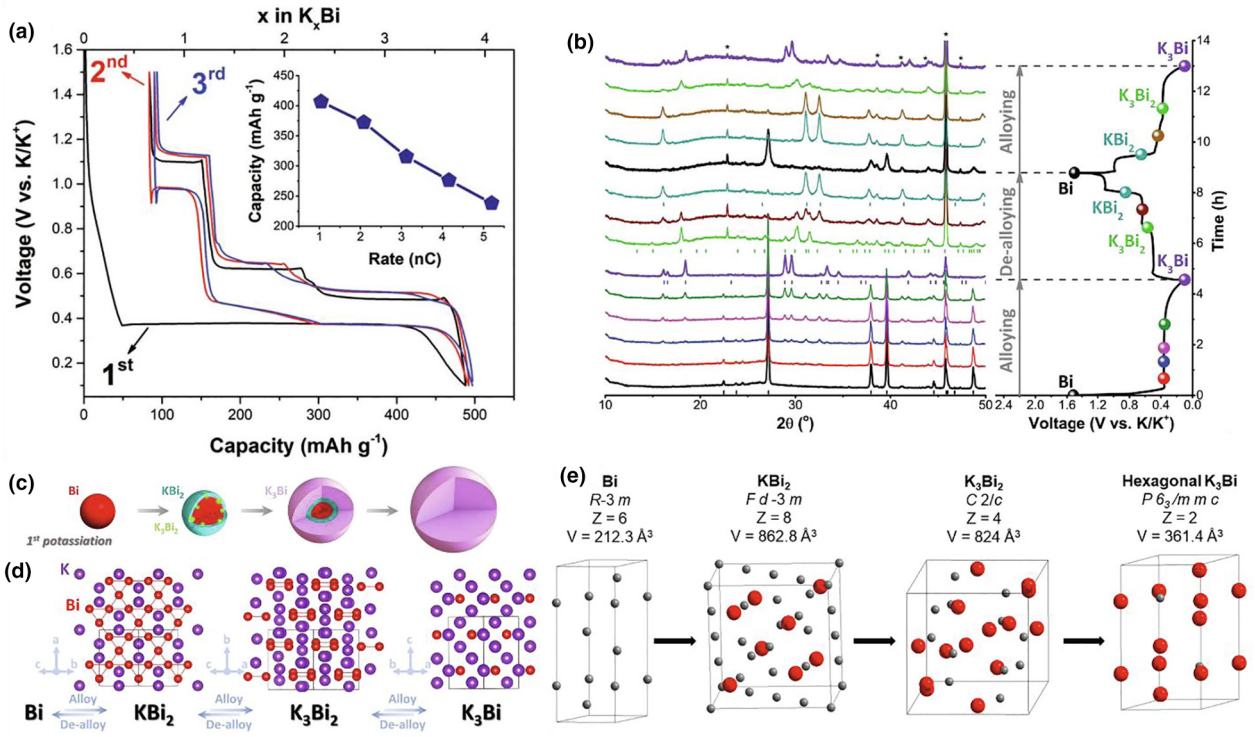

FIGURE 5

(a) Electrochemical curves of Bi electrode at 400 mA g^{-1} and the rate capability (inset) in 1 M KPF_6/diglyme electrolyte, (b) *In-situ* XRD patterns of the Bi electrode for the 1st charge–discharge and the 2nd charge process. Alloying and dealloying processes in Bi electrode in (c) The 1st discharge and (d) The following cycles. Reproduced with permission [105], © WILEY-VCH, 2018. (e) Crystal structures of phases observed during *operando* XRD for Bi. Reproduced with permission [67], © American Chemical Society, 2018.

ex-situ XRD Wu et al. [108] could only observe hexagonal K_3Bi after discharge to 0.01 V, despite the existence of discharge plateaus at 0.9 and 0.4 V. There is no proper evidence for this direct transformation of Bi to K_3Bi, however, they referred that this could be due to large overpotentials that accelerate the transition from Bi to K_3Bi. This might be a similar phenomenon as observed in case of sodiation of Bi by Gao et al. [109], where they were also unable to detect the NaBi phase during the whole discharge process due to the large overpotential, they attributed this to the short existence time of NaBi at the middle stage of discharge. However, the charge plateaus represented a transition from K_3Bi–K_3Bi_2, K_3Bi_2–KBi_2, and KBi_2–Bi, and the reverse process of the phase evolution during the second discharge [108]. Fig. 5e shows the potassiation of Bi with the crystal structures phases observed during *operando* XRD. In summary, the phase transition of bismuth can be described as follows, where ^{c}M represents crystalline [67].

^{c}Bi → ^{c}K$_3$Bi$_{(hex)}$ First Discharge

^{c}K$_3$Bi$_{(hex)}$ → ^{c}K$_3$Bi$_2$ → ^{c}KBi$_2$ → ^{c}Bi Charge

A very large volume expansion of ~400% is estimated on the formation of K_3Bi during potassiation of a Bi electrode, which inevitably results in pulverization of the anode and concomitant electrolyte consumption. Nano-structural engineering of the Bi anode, for example in the form of nanoparticles, nanosheets or as a hybrid structure with conductive matrices has been investigated to improve performance [101,103,110,111]. Qiao's group [112] synthesized a hybrid structure consisting of a carbon-coated double-shell Bi hollow box (C@DSBC). DSBC was obtained by using zeolitic imidazolate framework-8 (ZIF-8) cubes as a template followed by sulfidation, and zinc replacement with Bi, by a room temperature cation-exchange method. The carbon coating was carried out by the subsequent calcination with polydopamine Fig. 6a. The electrochemical performance of C@DSBC was compared with the micro-sized Bi in 2.0 M KFSI in 1,2-dimethoxyethane (DME). Fig. 6b–d show the charge/discharge profiles and cycling performance of C@DSBC and micro-sized Bi. It can be observed that C@DSBC showed a reversible capacity of 351 mAh g^{-1} with an initial Coulombic efficiency (CE) of 52%, which was lower compared to that of micro-sized Bi. The low initial CE of C@DSBC might be due to the irreversible reaction between surface functional groups of carbon and potassium. The cycling performance of C@DSBC exhibited reasonably good durability as it maintained the capacity of over 200 mAh g^{-1} after 200 cycles at 400 mA g^{-1} (1 C), compared to only 65 mAh g^{-1} for micro-sized bismuth. Specifically, a C@DSBC anode delivered capacities of 340, 302, 274, 251, and 222 mAh g^{-1} at 40, 80, 200, 400, and 800 mA g^{-1}, respectively. The origin of the improved capacity of C@DSBC was revealed by combining *operando* synchrotron-based XRD providing high temporal resolution with *ex-situ* X-ray absorption near-edge structure (XANES). It was concluded that the improved reversible capacity of nanostructured C@DSBC under low current density originated from numerous internal voids that were able to accommodate the large volume expansion. The improved capacity under high current density arose from the larger surface area, which offered

Please cite this article in press as: S. Imtiaz et al., Materials Today, (2021), https://doi.org/10.1016/j.mattod.2021.02.008

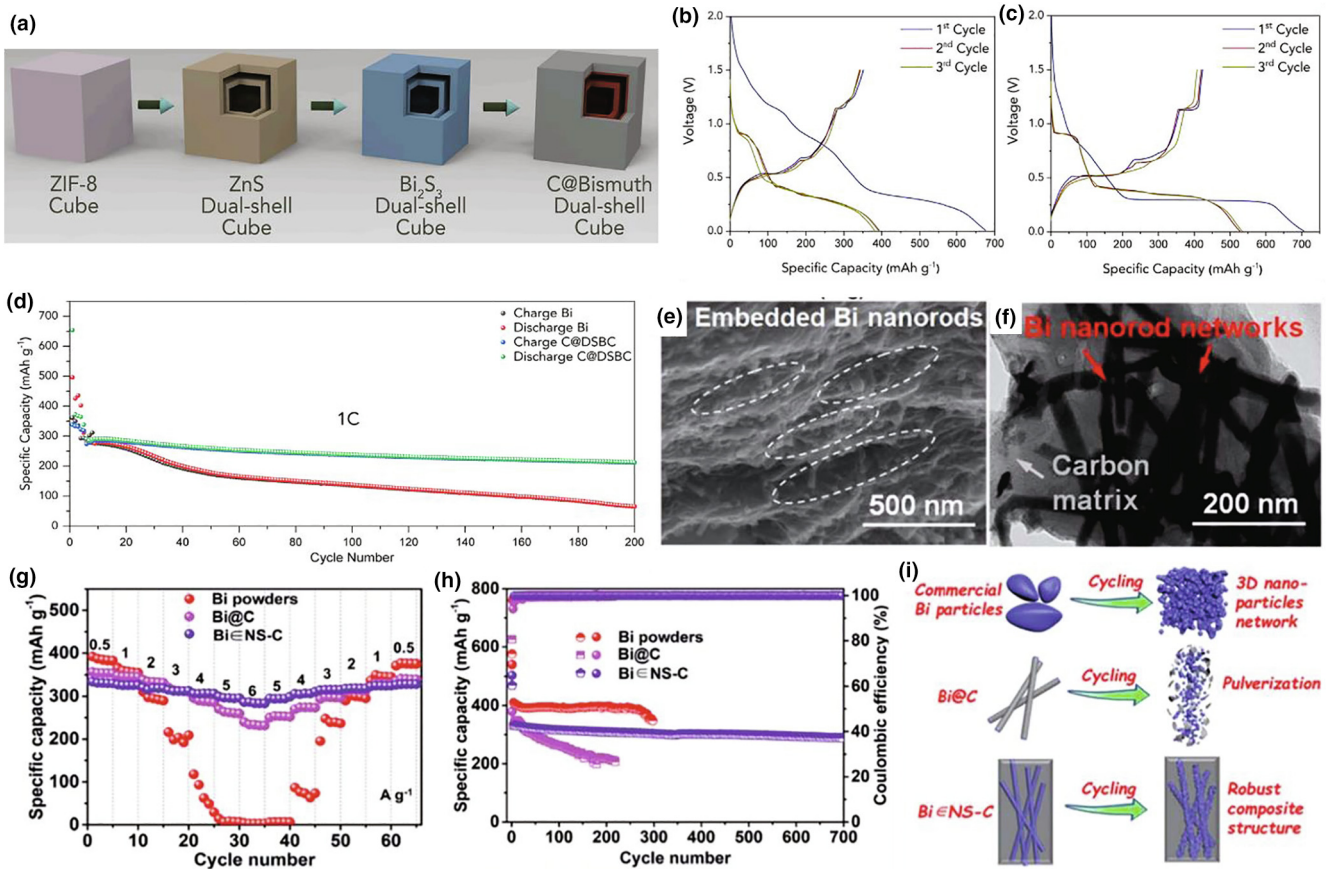

FIGURE 6

(a) Scheme illustrating the synthetic procedure of C@DSBC, (b) Initial cycling curves of C@DSBC and (c) Microsized Bi, (d) Long cycling performance of C@DSBC and microsized Bi. Reproduced with permission [112], © Elsevier Inc. 2019. (e) Cross-section SEM and (f) TEM images of Bi∈NS–C, (g) Rate performance and (h) Cycling stability of Bi powder, Bi@C, and Bi∈NS–C, and (i) Illustrations of the morphology evolution of the different samples in the repeated alloying/dealloying process. Reproduced with permission [113], © Royal Society of Chemistry, 2020.

more electrochemical active sites to react with K ions. Separately, Jiao et al. fabricated Bi nanorod networks confined in a N, S co-doped carbon matrix (Bi∈NS–C) via the formation of a Bi_2S_3 nanorod-containing gel precursor followed by pyrolysis under an Ar atmosphere [113]. Fig. 6e and f show the SEM (cross-section) and TEM images of Bi∈NS–C, which clearly indicate that the Bi nanorods were embedded in the carbon matrix. The electrochemical performance of the as-prepared samples was compared with commercial Bi powder and carbon-shelled Bi nanorods (Bi@C). Fig. 6g and 6 h shows that Bi∈NS–C displayed much improved rate performance and cycling stability, which was ascribed to the network structure of Bi nanorods accelerating the reaction kinetics and accommodating the large strain originating from the alloying/dealloying process. Furthermore, the robust carbon matrix not only served as a conductive skeleton but also buffered the large volume variation. The morphology evolution of the different samples in the repeated alloying/dealloying process is illustrated in Fig. 6i.

Recently, it was found that binary and ternary alloy systems facilitated an improved anode performance in comparison to the pure elemental counterparts by synergistically alleviating the volume expansion issues [114–116]. Among various Bi-based alloys, Bi-Sb alloys are the most common because of the similar physiochemical properties of Bi and Sb as well as their ability to form solid solutions (Bi_xSb_{1-x}) at any molar ratios. For example, a composite of Bi-Sb alloy nanoparticles embedded in porous carbon nanosheets (BiSb@C) was designed using a freeze-drying assisted in-situ pyrolysis method that employed a mixture of potassium antimonyl tartrate sesquihydrate, bismuth potassium citrate, and KCl as the template [117]. During freeze-drying, the metal salts were covered on the surface of KCl crystal particles, followed by pyrolysis, in which organic ligands of the metal salts were converted to amorphous carbon, along with reduction from Bi^{3+} and Sb^{3+} to form BiSb alloy particles. The TEM images in Fig. 7a indicated that the BiSb alloy nanoparticles were uniformly embedded within the carbon matrix. The high-resolution TEM image in Fig. 7b revealed that BiSb alloy nanoparticles had a crystalline core and an amorphous shell layer (the shell could be metal oxide formed in the synthesis process). The characteristic structure featuring both Bi and carbon, effectively suppressed the stress/strain of Sb caused by the volume expansion in the redox reaction. Benefitting from these robust structural features, the BiSb@C anode delivered a high reversible capacity of 320 mAh g^{-1} at 500 mA g^{-1} after 600 cycles, and a good rate capability of 152 mAh g^{-1} at 2000 mA g^{-1}. Furthermore, full cell PIBs featuring a Prussian blue cathode with the BiSb@C composite anode displayed a high capacity of 396 mAh g^{-1} (based on the mass of anode) with a

Please cite this article in press as: S. Imtiaz et al., Materials Today, (2021), https://doi.org/10.1016/j.mattod.2021.02.008

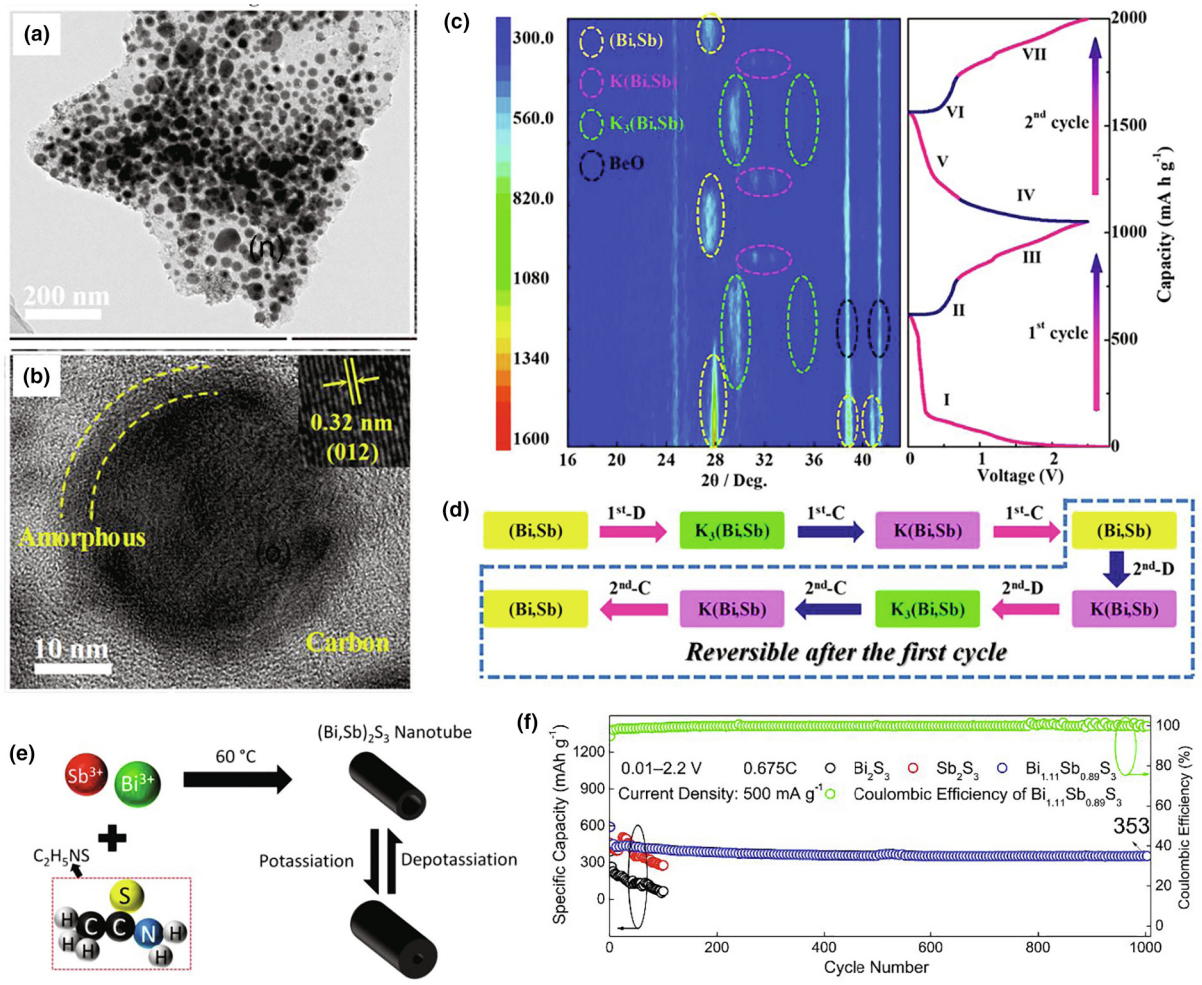

FIGURE 7

(a) TEM, and (b) HRTEM images of BiSb@C composite, (c) *Operando* XRD of the BiSb@C composite anode during the first and second cycles, and corresponding charge/discharge profiles for the BiSb@C composite electrode at 10 mA g^{-1} are also shown for reference (right). (d) Schematic of the potassiation/depotassiation process of the BiSb@C composite. Reproduced with permission [117] © American Chemical Society, 2019 (e) Synthesis procedure and (f) cycling performance of $(Bi,Sb)_2S_3$ nanotubes at 500 mA g^{-1}. Reproduced with permission [118] © American Chemical Society, 2019.

stable cycling life. *Operando* XRD measurements revealed the potassiation/depotassiation mechanism of the bimetallic alloy showing that the BiSb@C anode underwent an irreversible potassiation reaction from (Bi,Sb) to K_3(Bi,Sb) in the first discharge process and then reversible depotassiation/potassiation reactions from K_3(Bi,Sb) ↔ K(Bi,Sb) ↔ (Bi,Sb) in the following cycles (Fig. 7c and d). Lu and co-workers [118] reported a unique *in-situ* alloying strategy for obtaining homogeneous (Bi,Sb) alloy nanoparticles from $(Bi,Sb)_2S_3$ nanotubes by combining the synergistic properties of metal sulfides and bimetallic alloy systems (Fig. 7e). By using *operando* XRD, along with TEM and energy dispersive X-ray spectroscopy mapping, the phase evolution of (Bi, $Sb)_2S_3$ nanotubes could be separated into 6 stages, summarized in the following equations, where the reversibility of stage I and II is limited, while the stages III, IV, V, and VI are highly reversible.

$$(Bi, Sb)_2S_3 + K^+ + e \rightarrow Bi + Sb + K_2S_4\ (\sim 1.2\ V)\ (I)$$
$$Bi + Sb \rightarrow (Bi, Sb)\ (\sim 1.2\ V)\ (II)$$
$$(Bi, Sb) + K^+ + e \rightarrow K(Bi, Sb)\ (\sim 0.6\ V)\ (III)$$
$$K(Bi, Sb) + K^+ + e \rightarrow K_3(Bi, Sb)\ (\sim 0.2\ V)\ (IV)$$
$$K_3(Bi, Sb) - K^+ - e \rightarrow K(Bi, Sb)\ (\sim 0.6\ V)\ (V)$$
$$K(Bi, Sb) - K^+ - e \rightarrow (Bi, Sb)\ (\sim 1.2\ V)\ (VI)$$

The atomic-level *in-situ* alloying strategies produced a synergistic effect of Sb and Bi and yielded outstanding anode performance for PIBs, attaining a high specific capacity of 611 mAh g^{-1} at 0.135C and retaining 353 mAh g^{-1} over 1000 cycles at 500 mA g^{-1} (Fig. 7f). In addition, a full PIB with perylenetetracarboxylic dianhydride (PTCDA) cathode achieved a respectable capacity of 207 mAh g^{-1} (based on the mass of anode) after 100 cycles.

Sn-based anodes

Tin (Sn) is a well-known alloying anode material and has been intensively studied in LIBs and SIBs, theoretically providing specific capacities of 990 and 847 mAh g^{-1}, based on the formation of $Li_{22}Sn_5$ and $Na_{15}Sn_4$ as the final phase, respectively [57,119,120]. In fact, Sn was employed as an anode in commercial rechargeable batteries "Nexelion" by the Sony Corp. in Japan [121]. Sangster and Bale [122] reported a binary K-Sn phase diagram in 1998, demonstrating that a range of phases, such as K_2Sn, KSn, K_2Sn_3, K_2Sn_5, KSn_2, and K_4Sn_{23} are possible. Ceder's group predicted by DFT calculations that K can alloy with Sn

Please cite this article in press as: S. Imtiaz et al., Materials Today, (2021), https://doi.org/10.1016/j.mattod.2021.02.008

in a one-to-one ratio to form KSn, with a capacity of 226 mAh g^{-1} [123]. The first experimental report on the electrochemical behavior of a Sn-based anode in PIBs was reported by Sultana et al. [124]. A Sn–carbon (Sn/C) composite was prepared *via* mechanical ball-milling of 30 wt% of graphite and 70 wt% of Sn nanoparticles under an Ar atmosphere. The Sn/C composite anode displayed a reversible capacity of 150 mAh g^{-1}. The corresponding galvanostatic profile showed characteristic features mainly associated with a K alloying–dealloying reaction. Moreover, *ex-situ* XRD showed both the presence of crystalline phases such as K_2Sn_5 and K_4Sn_{23} upon discharge, and a decrease in intensity upon charge, suggesting a successful alloying/dealloying process of Sn and K. Nevertheless, the understanding of the reaction mechanism based on an ill-defined XRD pattern was not conclusive. Subsequently several studies reported potassiation/depotassiation mechanisms for the Sn/K system, mainly for β-Sn (white Sn with a tetragonal structure) [65,125]. Based on the *in-situ* TEM measurements, the potassiation of the Sn nanoparticles proceeded by a two-step mechanism [65]. By considering the evolution of volume change, it was suggested that a K_4Sn_9 phase formed during the first-step potassiation, and a KSn alloy after full potassiation. Ramireddy et al. [125] investigated the reaction mechanism of Sn by *in-situ* synchrotron XRD during CV scans (Fig. 8a). During the cathodic scan, the signals of Sn gradually decreased, as confirmed by the enlarged XRD patterns in Fig. 8b. At the end of the cathodic scan or potassiation, Sn is completely converted into the tetragonal K_4Sn_4 phase as XRD peaks obtained at *2θs* of 7.11°, 7.63°, 14.45°, 15.24°, 15.47°,

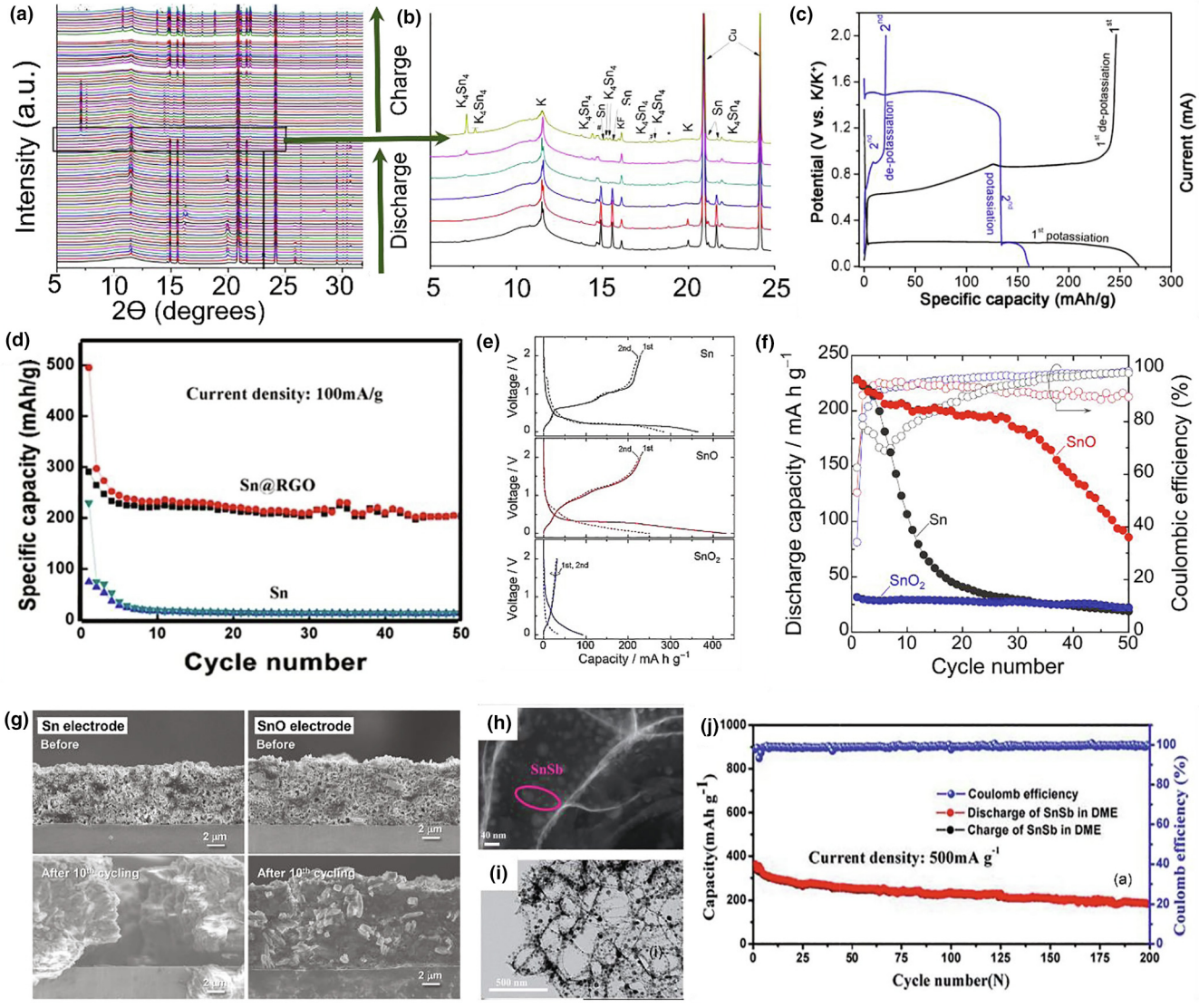

FIGURE 8

(a) *In-situ* XRD patterns during CV (b) Zoomed-in *in-situ* XRD patterns corresponding to the region associated with the phase transformation of primary interest during electrochemical potassiation of Sn, (c) Chronopotentiograms of 1 μm thick Sn film in a K cell at a current density of 25 mA g^{-1}. Reproduced with permission [125], © The Electrochemical Society, 2017. (d) Cycling performance comparison of Sn and Sn@RGO at 100 mA g^{-1}. Reproduced with permission [128], © Elsevier Ltd. 2019 (e) Initial charge–discharge (K-insertion/extraction) profiles of Sn, SnO, and SnO_2, (f) Cycling performance of Sn, SnO, and SnO_2 electrodes in 0.5 M KPF_6/EC:DEC, (g) Cross-sectional FE-SEM images of Sn-based electrodes before and after the 10th cycle at 25 mA g^{-1}. Reproduced with permission [129], © American Chemical Society, 2018. (h) FE-SEM (i) TEM images, and (j) Cycling performance of 3D SnSb@NC at at 500 mA g^{-1}. Reproduced with permission [130], © Royal Society of Chemistry, 2019.

Please cite this article in press as: S. Imtiaz et al., Materials Today, (2021), https://doi.org/10.1016/j.mattod.2021.02.008

17.21°, 18.03 ° and 22.42 °, corresponding to the reversible capacity of 245 mAh g^{-1} in the first cycle, with the intensities of the β-Sn peaks diminishing considerably. During the anodic scan, K_4Sn_4 peaks become weaker and disappeared at ~0.98 V; finally, peaks of β-Sn started to reappear. The results indicated that upon potassiation KSn formed *via* a one-step phase transformation without the formation of an intermediate phase reverting to β-Sn after de-potassiation. However, their observations were not entirely consistent with their discharge/charge profiles (Fig. 8c) which showed at least two plateaus in the profile. This inconsistency might be due to the weaker signals from the intermediate phases and the relatively short residence times. The ambiguity of the electrochemical K-alloying mechanism of Sn was later clarified by Stievano and co-workers [115] by low temperature *ex-situ* ^{119}Sn Mössbauer spectroscopy combined with first principles calculations. The results proved the formation of KSn at the end of potassiation of β-Sn, and an intermediate K_4Sn_9 phase during depotassiation. In summary, the alloying/dealloying path of β-Sn and K can be written as;

$$\beta - \mathrm{Sn} \overset{potassiation}{\rightarrow} KSn(discharge)$$

$$KSn \overset{depotassiation}{\rightarrow} K_4S_9 \overset{depotassiation}{\rightarrow} \beta - \mathrm{Sn(Charge)}$$

The initial reports using a Sn anode in PIBs showed very limited cycling performance with rapid capacity fading caused by significant pulverization [65]. Ramireddy et al. [125] observed many cracks by SEM on β-Sn electrodes after the first potassiation, where the Sn anode was found to be severely fractured, with aggregation and delamination observed after the 2nd potassiation, leading to rapid capacity fade. Also, poor cyclic stability of a pure 1 μm thick Sn film was found when cycled between 2.00 to 0.01 V, which was thought to be due to irreversible surface phenomena at higher potentials of ~1.3–1.4 V. However, the galvanostatic cycling within a restricted cell voltage window of 1.20–0.01 V displayed a much better cyclic stability (85 mAh g^{-1} at the end of 20 cycles). Similar to other alloy-based materials, the large volume expansion of ~197% resulting from the KSn formation is a serious issue, which leads to the growth of an unstable solid electrolyte interface (SEI) layer and pulverization of the material, resulting in significant capacity fade. As already mentioned in section 'Sb-based anodes', introduction of carbon materials helps avoid structural degradation, improves the conductivity, and also enhances the surface of the electrode for better reaction kinetics [126,127]. For this reason, Wang et al. [128] encapsulated submicron metallic Sn particles in an RGO network (Sn@RGO). Sn@RGO was obtained by drying a suspension of GO in the presence of an $SnCl_4$ precursor via vacuum freeze-drying, followed by thermal reduction in Ar/H_2 atmosphere. The unique structure offered several advantages, including larger interlayer space to accommodate volume expansion, and enhanced structural integrity from absorbing stress during alloying/dealloying. It also provided a larger surface area for more active sites for redox reaction and inhibited the self-aggregation of Sn submicron particles. Owing to these advantages, the Sn@RGO composite provided a specific charge capacity of 200 mAh g^{-1} after 50 cycles, being much higher than that of pure Sn that showed only 12.9 mAh g^{-1} (Fig. 8d). Shimizu et al. [129] demonstrated that the use of Sn-based oxide electrodes instead of metallic-Sn as another promising strategy to improve the cycling performance. X-ray photoelectron spectroscopy (XPS) and XRD results showed that metallic-Sn and potassium oxide (K_2O) formed in the first charge (reduction) process of SnO, followed by reversible alloying reactions between the resulting Sn and K. The first conversion reaction was irreversible, but the alloying reaction of Sn to KSn was reversible. Interestingly, the SnO anode displayed a reversible capacity of ~230 mAh g^{-1}, very close to that of metallic-Sn (Fig. 8e), while SnO_2 showed little electrochemical reactivity to potassium because SnO_2 could not be completely reduced to Sn. The miniscule capacity observed in Fig. 6d was presumably due to a pseudo-capacitance. It was found that the retransformation of SnO rarely takes place under the upper cutoff voltage of 2.0 and 3.0 V, thus the potassium storage mechanism of SnO is like metallic-Sn, except for the first conversion reaction. The cycling performance displayed in Fig. 8f shows a rapid capacity fading for Sn, because of electrode disintegration induced by the significant volume change during K-Sn alloying/dealloying reactions, which was also confirmed by cross-sectional field-emission SEM (FE-SEM) images after 10 cycles (Fig. 8g). But the SnO electrode exhibited a reversible capacity of 183 mAh g^{-1} (80% capacity retention) after the 30th cycle, with no cracking or delamination of the electrode observed (Fig. 8g) even though the thickness was slightly increased. The relatively better cycling performance of SnO was attributed to the irreversible formation of amorphous-like K_2O matrices after the first cycle, which either acted as a buffer to relieve stresses induced by the volumetric change or suppressed Sn aggregation.

As previously discussed, the formation of bimetallic alloys has been shown to be a valid strategy to improve the capacity retention of alloying anodes and this is also the case for Sn [131]. Unlike β-Sn, which gives an abrupt capacity fade from the 1st cycle, a capacity retention of 75% was sustained by SnSb alloy after 40 cycles [115]. Recently, Wang et al. [130] confined an SnSb alloy in N-doped 3D porous carbon (3D SnSb@NC) *via* a facile NaCl-template assisted *in-situ* pyrolysis strategy. The high magnification FE-SEM and TEM images of the 3D SnSb@NC are shown in Fig. 8h and i, which indicate that numerous ultra-small sized particles were embedded in the thin carbon layer with a uniform pore structure. Owing to the synergistic effect of Sn and Sb, the uniformly anchored SnSb nanoparticles could effectively buffer the large volume expansion during charge/discharge. Furthermore, the N-doped 3D porous carbon provided active sties for redox reaction and facilitated the electrolyte penetration. As a result, the 3D SnSb@NC anode immersed in a DME electrolyte showed a high reversible capacity of 357.2 mAh g^{-1} at 50 mA g^{-1} and maintained 80% capacity after 200 cycles at 500 mA g^{-1} (Fig. 8j).

P-based anodes

Phosphorus (P) is a light nonmetallic element of group 15, and an attractive anode candidate for high energy density PIBs owing to its high abundance and large K^+ uptake capability [23,59,132]. Sangster studied the K-P phase diagram and reported that a range of alloys are possible during the alloying reaction of K with P, such as K_3P, K_4P_3, KP, K_4P_6, K_3P_7, K_3P_{11}, and KP_{15} [133]. Theoretically, based on a three-electron reaction mechanism, phospho-

Please cite this article in press as: S. Imtiaz et al., Materials Today, (2021), https://doi.org/10.1016/j.mattod.2021.02.008

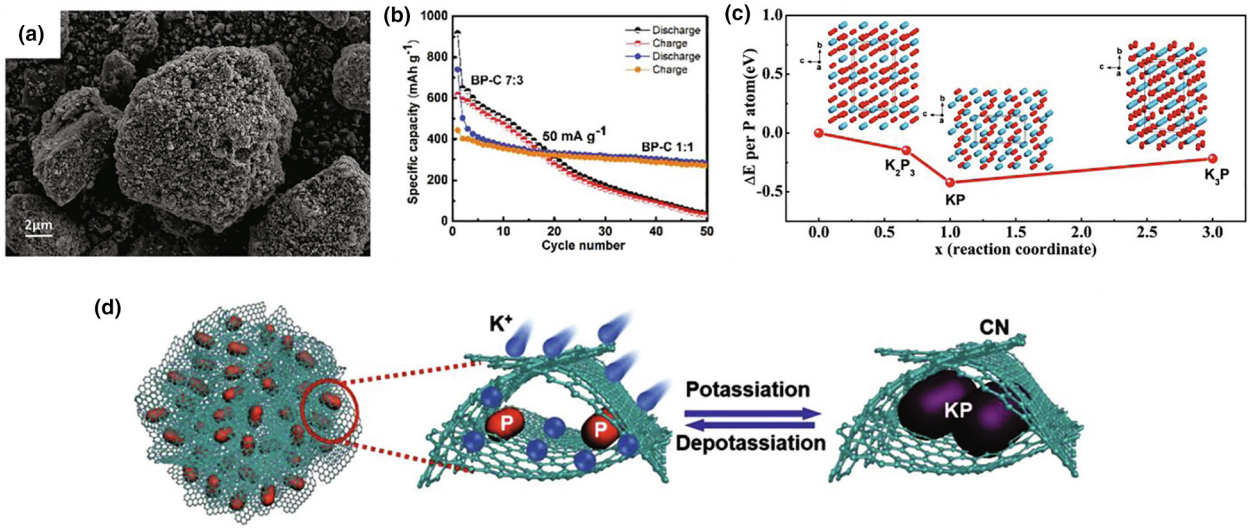

FIGURE 9

(a) SEM image of the BP-C composite, (b) Cycling performance of the BP–C 7: 3 and BP–C 1: 1. Reproduced with permission [69], © Royal Society of Chemistry, 2017 (c) Calculated formation energy (d) Schematic illustration of the charge/discharge process of the red P@CN composite electrode. Reproduced with permission [139], Wiley-VCH. 2018.

rus can provide an extremely high capacity of 2596 mAh g^{-1}, assuming the formation of K_3P [123]. However, up to now, no experimental evidence has reported the presence of K_3P, and the K-storage mechanism is still unclear. Zhang et al. [134] proposed *via ex-situ* XRD that partly crystalline or amorphous $K_{3-x}P$ could be a final discharge product, whereas Kim et al. revealed that KP and K_4P_3 are the most stable phases of the alloying process, corresponding to much lower theoretical capacity of 865 and 1154 mAh g^{-1}, respectively [123]. Even with the formation of the KP phase, P is a promising alloying anode material for use in PIBs, as the theoretical capacities are still higher than most alloy type (Sb, Sn, Bi, Ge, Pb) anode materials. P mainly has three allotropes, which are white, red, and black. Among them, white P is not suitable for anode application because of toxicity and spontaneous combustion in air. By contrast, black and red P are chemically stable at room temperature. Regardless of the high abundance and low cost of red P, its low electronic conductivity (10^{-14} S cm^{-1}) leads to reduced electrochemical redox reactions [59,135]. Black P has a 2D layered structure similar to graphite and displays better electron mobility than red P [136,137]. In view of the high theoretical conductivity and robustness in the crystal structure of P-based anodes, both red and black P have been employed in PIBs.

Unfortunately, like other alloy-based anode materials, P also faces the huge volume change during alloying/dealloying process resulting in a rapid capacity fade and sluggish kinetics. Thus, advanced structural engineering of P is necessary to alleviate the structural strains, buffer the volume expansion, and facilitate charge transfer and ionic diffusion [138]. Zhang et al. [134], for instance, synthesized a red phosphorus-carbon (P/C) composite anode by a conventional and scalable ball-milling technique. The composite mainly consisted of irregular agglomerated micrometer sized particles. When applied as an anode in PIBs, it exhibited a very high initial capacity of 2171.7 mAh g^{-1} at 50 mA g^{-1}, with a proposed reaction mechanism that suggested formation of a $K_{3-x}P$ alloy. However, the capacity decayed very fast, to 480 mAh g^{-1} after the 3rd cycle and to zero within ~40 cycles. In another approach, Sultana et al. [69] prepared black P via mechanical milling of red P in a planetary ball mill, and then encapsulated black P into the carbon matrix (BP-C). The SEM image of BP-C nanocomposite showed a range of secondary aggregated particles with the sizes between hundreds of nanometers and tens of micrometers (Fig. 9a). The BP-C composites were prepared in two different ratios denoted as BP–C 7:3 and BP–C 1:1. The BP–C 7:3 sample with a higher P content showed a high capacity of 617 mAh g^{-1} in the first cycle, but it decreased in the following cycles. For the BP–C 1:1 sample with a lower content of P, the initial capacity was lower (443 mAh g^{-1}) but much more stable, as demonstrated in Fig. 9b. Based on *ex-situ* XRD analysis, the KP alloy was detected as the end product of the electrochemical transformation ($P + K^+ + e^- \leftrightarrow KP$ was proposed as the reaction mechanism), which was different from the study conducted by Zhang et al. [134]. To clarify the potassium storage mechanism, Xiong et al. [139] prepared a red P@CN composite by anchoring red P nanoparticles on a 3D carbon nanosheet framework, which was analyzed using TEM supported with DFT calculations. Fig. 9c shows the calculated formation energy; the lowest formation energy (−0.421 eV, per mole P) was observed for the KP phase, while it was larger for K_2P_3 (−0.148 eV) and K_3P (−0.218 eV), suggesting that the KP Phase is thermodynamically more stable than K_2P_3 and K_3P. The TEM selected area electron diffraction (SAED) results experimentally correlated the one-electron reaction mechanism with the formation of the KP phase at full potassiation, corresponding to a volume expansion of 241% and a capacity of 843 mAh g^{-1} (the theoretical capacity of KP is reported as 843 mA h g^{-1} in many articles, however, the correct value should read as 865 mAh g according to the corrected reference [140]). Additionally, the red P@CN composite demonstrated a high reversible capacity of 655 mAh g_P^{-1} at 100 mA g^{-1} but dropped to 427.4 mAh g_P^{-1}

Please cite this article in press as: S. Imtiaz et al., Materials Today, (2021), https://doi.org/10.1016/j.mattod.2021.02.008

after 40 cycles. Fig. 9d illustrates the charge/discharge process of the red P@CN electrode.

Recently, Yu and co-workers [141] embedded red P into free-standing N-doped porous hollow carbon nanofibers (red P@N-PHCNFs). The schematic of the experimental procedure and corresponding microstructure of the obtained red P@N-PHCNFs is illustrated in Fig. 10a. Polycaprolactone nanofibers were first fabricated by electrospinning and then used as a sacrificial template to create hollow polypyrrole nanofibers, followed by a chemical activation process with potassium hydroxide to generate N-doped porous hollow carbon nanofiber matrix (N-PHCNFs). Finally, red P was infiltrated into the N-PHCNFs by a vaporization-condensation strategy to obtain the red P@N-PHCNFs. For comparison, hollow carbon fibers coated with red P (red P/N-HCNFs) were also prepared. The scanning transmission electron microscopy (STEM) image and corresponding elemental mapping of the red P@N-PHCNFs composite confirmed the homogeneous distribution of red P, N and C (Fig. 10b–e). The red P@N-PHCNFs anode delivered a high capacity over 700 mAh g^{-1} at 0.1 A g^{-1} in the first 15 cycles which was maintained at 650 mAh g^{-1} after 100 cycles. However, the red P/N-HCNFs composite, in which red P occurred mainly on the outer

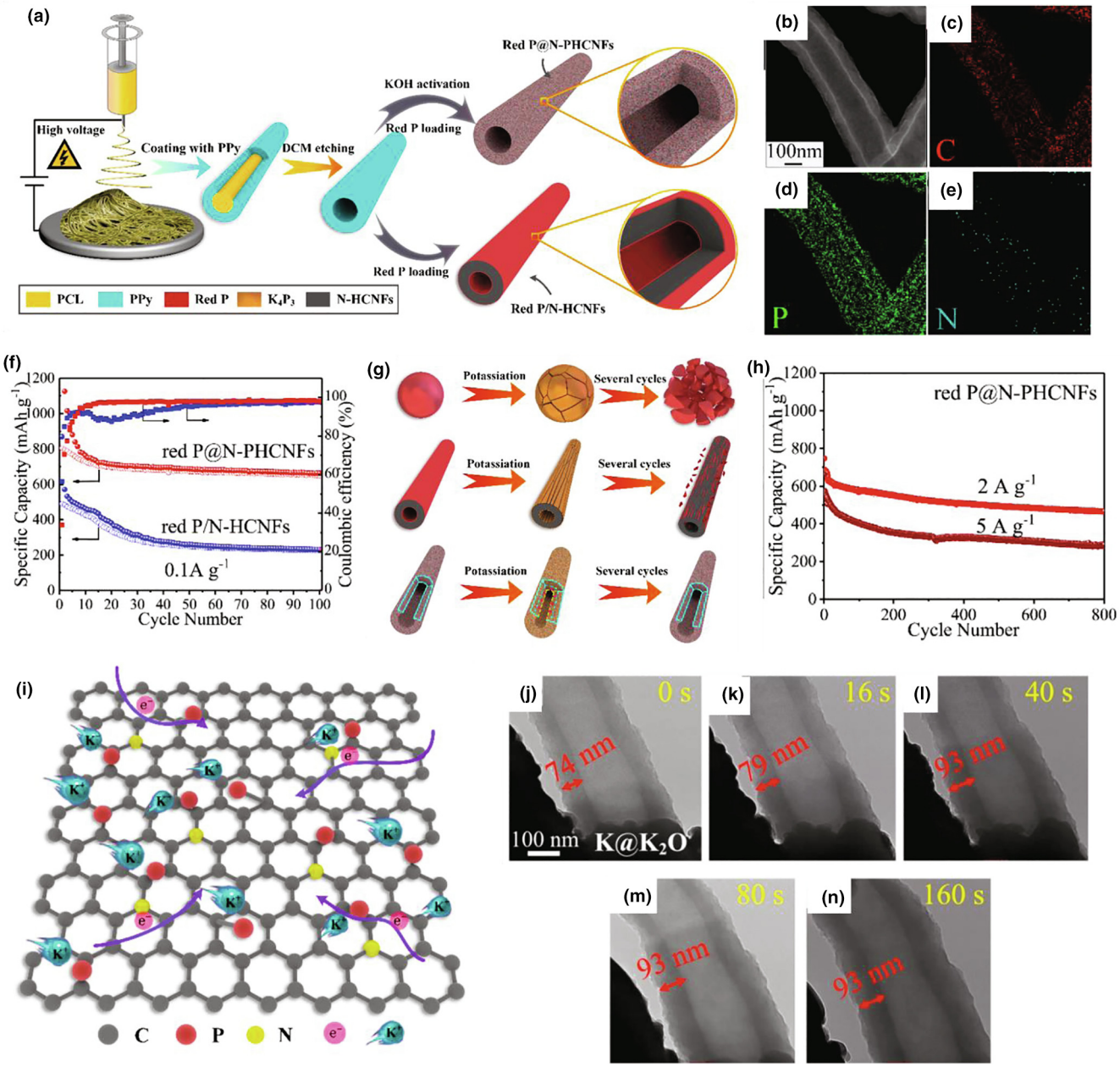

FIGURE 10

(a) Schematic of experimental procedure and corresponding microstructure of red P@N-PHCNFs and red P/N-HCNF Sample, (b) STEM image of red P@N-PHCNFs and the corresponding elemental mapping of (c) C, (d) P, and (e) N elements, (f) Cycling performance of the red P@N-PHCNFs and red P/N-HCNFs anodes at 0.1 A/g, (g) Schematic illustration of the potassiation/depotassiation of red P Particles, red P/N-HCNFs, and red P@N-PHCNFs, (h) Cycling performance of the red P/N-HCNFs at different current density, (i) Schematic of P-C Chemical Bonds and N-Doping in red P@N-PHCNFs, and (j-n) Time-lapse TEM images for a single red P@N-PHCNFs during potassiation process. Reproduced with permission [141], © American Chemical Society, 2019.

Please cite this article in press as: S. Imtiaz et al., Materials Today, (2021), https://doi.org/10.1016/j.mattod.2021.02.008

and inner surface of hollow carbon nanofiber matrix showed a fast capacity fade after a few cycles, after which only the capacity contribution of the carbon matrix remained (Fig. 10f). This fast capacity decay of red P/N-HCNFs after a few cycles was attributed to the severe pulverization and the loss of contact with the hollow carbon matrix due to the volume expansion. However, the good capacity and stability of the red P@N-PHCNFs composite was ascribed to the large surface area and high pore volume, which avoided the problems of pulverization. A schematic illustration of the potassiation/depotassiation of red P particles, red P/N-HCNFs, and red P@N-PHCNFs is shown in Fig. 10g. In addition, the red P@N-PHCNFs anode displayed unprecedented long cycle life with high reversible capacity of 465 mAh g^{-1} at 2 A g^{-1} after 800 cycles and very good rate capability of 342 mAh g^{-1} at 5 A g^{-1} (Fig. 10h). The strong P-C chemical bond and N-doping in the hollow carbon fiber was also considered another promoting factor, which provided enhanced adsorption energy and better contact between red P and the porous N-PHCNFs matrix and facilitated K^+ diffusion and charge transfer (Fig. 10i). *In-situ* TEM investigation showed that the thickness of the red P@N-PHCNFs reached 93 nm versus the initial 74 nm upon potassiation (Fig. 10j-n), corresponding to a volume expansion of only 26%, which is significantly less than for other alloy-type anode materials, and the red P@N-PHCNFs exhibited a stable structural change without any cracking and fracture. By combining *ex-situ* XRD and *in-situ* Raman analysis, K_4P_3 was proposed as the final potassiation product of red P, and thus a reaction mechanism of $4\,K + 3P \leftrightarrow K_4P_3$, with a corresponding theoretical capacity of 1154 mAh g^{-1}.

Another form of phosphorus that is considered promising for achieving high capacity is the 2D allotrope, phosphorene. Phosphorene has a layered structure with the atomic layers bound *via* van der Waals forces, which can be fabricated by direct exfoliation of black P [142,143]. In contrast to other 2D materials such as MXenes and graphene, phosphorene displays a low diffusion barrier and high energy densities [132]. In addition, compared to BP, phosphorene provides high specific surface area, short and effective ion diffusion channels, high carrier mobility, superior mechanical flexibility, and high energy storage efficiency of active sites [144,145]. However, the inherently low electrical conductivity of phosphorene and structural deformation, due to the large radius of the K^+, pose challenges for its application in PIBs. A few-layer phosphorene (FLP) electrode was fabricated by Koratkar's group *via* liquid phase exfoliation of bulk black P. FLP showed an initial high specific capacity of ~1200 mAh g^{-1}, with rapid capacity decay in subsequent cycles, attributed to pulverization of the anode due to large volume changes during the alloying/dealloying of phosphorene. *Ex-situ* XRD characterization combined with DFT calculations confirmed the formation of K_4P_3 in FLP at ~0.03 V [146].

The tin/phosphorus Sn_4P_3 alloy is another potential alloying anode material for use in PIBs because of providing the synergistic effect between P (high capacity) and Sn (high conductivity) [147,148]. Guo's group [149] studied the electrochemical performance and reaction mechanism of Sn_4P_3, synthesized by a ball-milling process using elemental Sn and red phosphorus with the Sn_4P_3 particles then confined in N-doped carbon fibers through an electrospinning technique to obtain Sn_4P_3@carbon fibers. They confirmed by STEM that Sn_4P_3 particles of 400–500 nm diameters were well embedded in the carbon fibers. A relatively high rate capacity of 160.7 mAh (g. $Sn_4P_3)^{-1}$ was observed with the as-obtained Sn_4P_3@carbon fibers at 500 mA g^{-1} even after 1000 cycles. By using an *operando* XRD mechanistic study, the reaction mechanism of Sn_4P_3 was revealed as follows.

$$Sn_4P_3 + 3K_x \leftrightarrow 4Sn + 3(P - K_x)(\text{amorphous}) \quad (1)$$

$$11(P - K_x) + yK \leftrightarrow K_3P_{11}(11_{x+y=3}) \quad (2)$$

$$K_3P_{11} + Sn + 31K \leftrightarrow KSn + 11K_3P \quad (3)$$

In the first discharged phase, Sn_4P_3 broke down into Sn and the P components precipitated into an amorphous form to react with potassium (1). Upon potassiation, first K_3P_{11} is formed (2), after which Sn alloyed completely with K to form the KSn phase (3), and K_3P_{11} was further potassiated to form the K_3P phase (Fig. 11). Thus, the synergistic K^+ storage of K-Sn and K-P phases provided a higher capacity, and possibly acted as a mutual buffer to alleviate the abrupt volume expansion during cycling. The group further extended their studies on the effects of electrolyte salt chemistry and additives on Sn_4P_3 alloy, which will be discussed in section 'Electrolytes and binders'. Furthermore, the study of alloying methods is not limited to those elements that form alloys with each other. Recent work by Sultana et al. [79] showed that simple ball milling of black P and Sb largely improved the electrochemical performance, even though these two components do not alloy with each other. These types of mixtures that are active with K, provide improved cycling behavior, possibly due to the different potential of the elements, thus, avoiding the abrupt simultaneous expansion/contraction of the electrode [150].

Si-based anodes

Silicon (Si) is considered as the most promising alloying anode material and has been intensively studied as an anode material in LIBs, owing to its high abundance (27% in the earth's crust), low cost, and ultrahigh specific capacity (3579 mAh g^{-1} for $Li_{3.75}$-Si alloy) [87,151]. However, its behavior is entirely different in SIBs and PIBs. It was proposed by Ceder's group that Si can alloy with potassium to form KSi, providing a theoretical capacity of 954 mAh g^{-1} [123]. This process was anticipated to provide a range of intermediate alloys, such as $K_{12}Si_{17}$, K_7Si_{46}, K_8Si_{46} and KSi. However, Sultana et al. [57] found no convincing evidence for potassiation of a Si/graphene electrode, and rather than alloying-dealloying they found that the charge/discharge profile exhibited capacitive behavior, with the graphene being the main contributor to the capacity (Fig. 12a). Furthermore, XRD data indicated the absence of any K_xSi_y compounds (Fig. 12b). These results were further confirmed by the electrochemical performances of pure Si and graphene electrodes, which exhibited tiny capacities for pure Si, and a reasonable capacity of 120–200 mAh g^{-1} over the first 50 cycles for the graphene electrode. These experimental results suggest that crystalline Si is probably inert toward the alloying with K (Fig. 12c and d). To the best of our knowledge, the only current report demonstrating electrochemical activity of Si for K-ion alloying is by Kubota et al. [26], in which they showed a capacity of 510 mAh g^{-1} after the

Please cite this article in press as: S. Imtiaz et al., Materials Today, (2021), https://doi.org/10.1016/j.mattod.2021.02.008

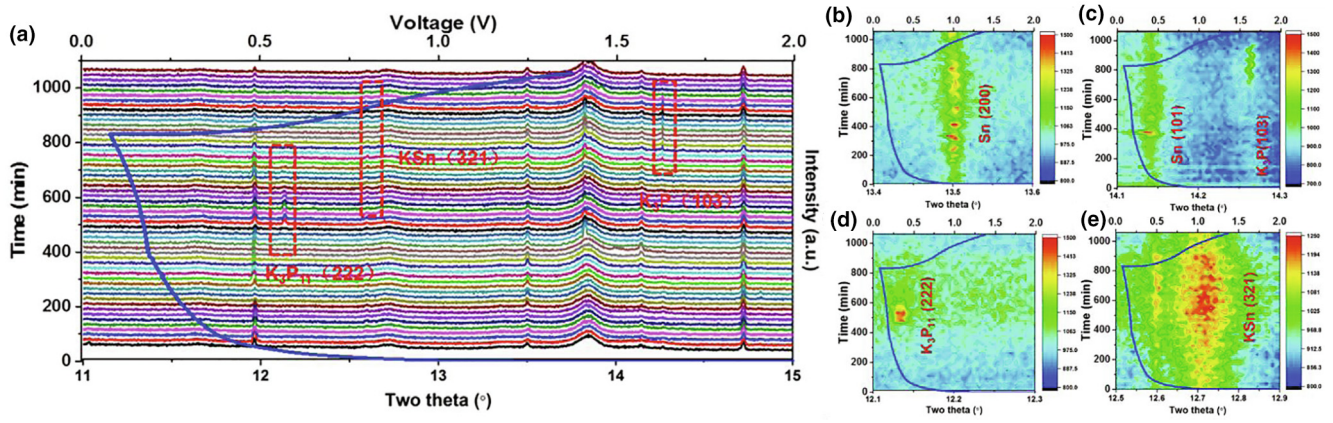

FIGURE 11

(a) In *operando* synchrotron XRD patterns of Sn_4P_3, and (b–e) Contour plots with superimposed voltage profiles shown for selected 2Θranges. (b) Sn (200), (c) Sn (101), (d) K_3P11 (222), and (e) KSn (321). Reproduced with permission [149], © Elsevier Inc. 2018.

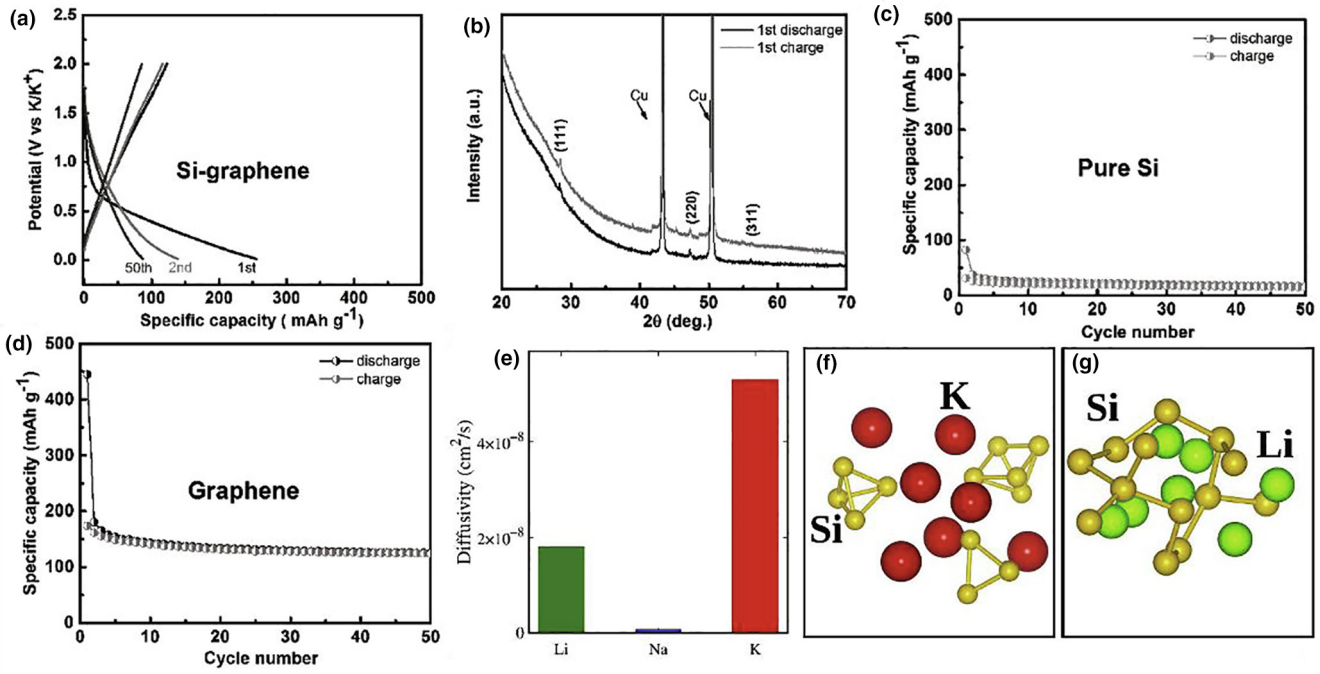

FIGURE 12

(a) Charge–discharge profiles for a Si-graphene electrode, (b) XRD patterns of the Si-graphene electrode after the first discharge and charge of the, capacity versus cycle number of (c) Pure Si, and (d) Graphene electrode. Reproduced with permission [57] © Wiley-VCH, 2017. (e) Diffusivities of Li, Na, and K in amorphous $Li_{3.7}Si$, $Na_{0.75}Si$, and $K_{1.0}Si$ at $T = 300$ K, respectively. Local structures around Si atoms corresponding to major Si-Si-Si bond angles in amorphous KSi (f) and in amorphous LiSi (g). The red, green, and yellow spheres represent K, Li, and Si atoms, respectively. Reproduced with Permission [63] © Elsevier B. V., 2019.

5th cycle for a nano-sized Si/graphite composite with sodium polyacrylate (PANa) binder, although no detailed reaction mechanism was provided.

Recently, it is reported that potassiation of crystalline Si (c-Si) is thermodynamically unfavorable, as the formation energy for KSi alloy is positive. On the other hand, alloying-dealloying of amorphous Si (a-Si) with potassium is possible. Lee and colleagues [63] considered the potassiation of a-Si using first-principles MD simulations. They determined that it is theoretically possible that a-Si can store 1.1 K ions per Si atom ($K_{1.1}Si$), corresponding to a capacity of 1049 mAh g^{-1}. Despite the large size of K^+, their diffusivity in a-Si was calculated to be very rapid at 5.3×10^{-8} cm^2 s^{-1}, which is almost two orders of magnitude higher than found for Na-ions (7.2×10^{-10} cm^2 s^{-1}) and even three times higher than that for Li-ions (1.8×10^{-8} cm^2 s^{-1}) (Fig. 12e). They attributed this proposed fast K-ion transport to a fairly high carrier ion concentration, weak electrostatic K-Si attraction and formation of isolated small Si_n clusters during the potassiation process in the form of triangle (Si_3), tetrahedron (Si_4), and pyramid (Si_5) structures (Fig. 12f and g). This K-induced

Please cite this article in press as: S. Imtiaz et al., Materials Today, (2021), https://doi.org/10.1016/j.mattod.2021.02.008

clustering of Si atoms can lead to a reduction of the number of attractive Si atoms around a K ion, thereby enhancing the kinetics of K ions. Nevertheless, currently there is very limited literature available on Si alloying anodes for PIBs with no experimental confirmation of capacity of Si, and there is huge scope for considerably more studies to find out experimentally whether Si is able to alloy with K and understand its alloying mechanism in PIBs.

Ge-based anodes

Germanium (Ge) alloying with K is predicted to take up to one K atom per germanium (KGe) upon potassiation, delivering a capacity of 369 mAh g^{-1} [123]. Despite the high cost of Ge, it has been intensively studied in LIBs because of its low mass, and 400 times higher ion diffusivity and 100 times higher electrical conductivity than Si [151–153]. In contrast Ge has been the subject of very limited studies in PIBs so far. Guo's group [154] confirmed for a layered GeP_5 electrode that Ge alloys with K to form KGe in an *operando* XRD study. Pure nanoporous germanium (np-Ge) samples have been synthesized by a facile chemical dealloying process using Al as sacrificial metal and studied as an anode for PIBs [64]. It was found that structural tailoring is essential to obtain practical capacities of Ge, and the anode with small ligaments (<100 nm) and interconnected nanopores showed stable capacity of 120 mAh g^{-1} over 400 cycles, which accounted for the potassiation degree of $K_{0.35}Ge$. Further, elemental mapping confirmed the formation of a K-Ge alloy after potassiation. Therefore, further analysis on the potassiation process of Ge is required to identify the exact potassiated phase. A layered Ge material, germanane, obtained from topotactic deintercalation of Ca^{2+} from a $CaGe_2$ Zintl phase has also been reported as an anode for PIBs [155]. The systematic study of germanane in different electrolytes demonstrated the importance of the electrolyte for anode evaluation in PIBs. Germanane exhibited remarkable capacity loss (<50 mAh g^{-1}) in 1 M KPF_6 in EC/dimethyl carbonate (DMC) with 1% fluoroethylene carbonate (FEC), and 1 M KFSI in EC/DMC with 1% FEC (Fig. 13a, b). However, it showed promising results in alternative electrolyte formulations including 0.8 M KPF_6 in 1:1 EC/DEC, and with 0.8 M KFSI in 1:1 EC/DEC (Fig. 13c, d). The 2nd discharge for these two formulations were 202 and 205 mAh g^{-1}, respectively, with stable cycling obtained for the 0.8 M KFSI in 1:1 EC/DEC electrolyte composition.

Pb-based anodes

Lead (Pb) can alloy with potassium leading to a theoretical capacity of 129 mAh g^{-1} [123], although its use has mostly been neglected as an anode material because of its high weight and toxicity. Pb metal foil was examined as an anode in a K-ion-based dual-ion battery (K-DIB) combining expanded graphite as the cathode and using 1 M KPF_6 in EC:DMC:ethyl methyl carbonate (EMC) = 4:3:2 (by volume) electrolyte. This cell showed a specific capacity of 71 mAh g^{-1} after the 10th cycle, but the cyclic stability was worse than Sn-foil anodes, also used in their study, so the detailed reaction mechanism of Pb was not investigated [156]. Gabaudan et al. [70] investigated the electrochemi-

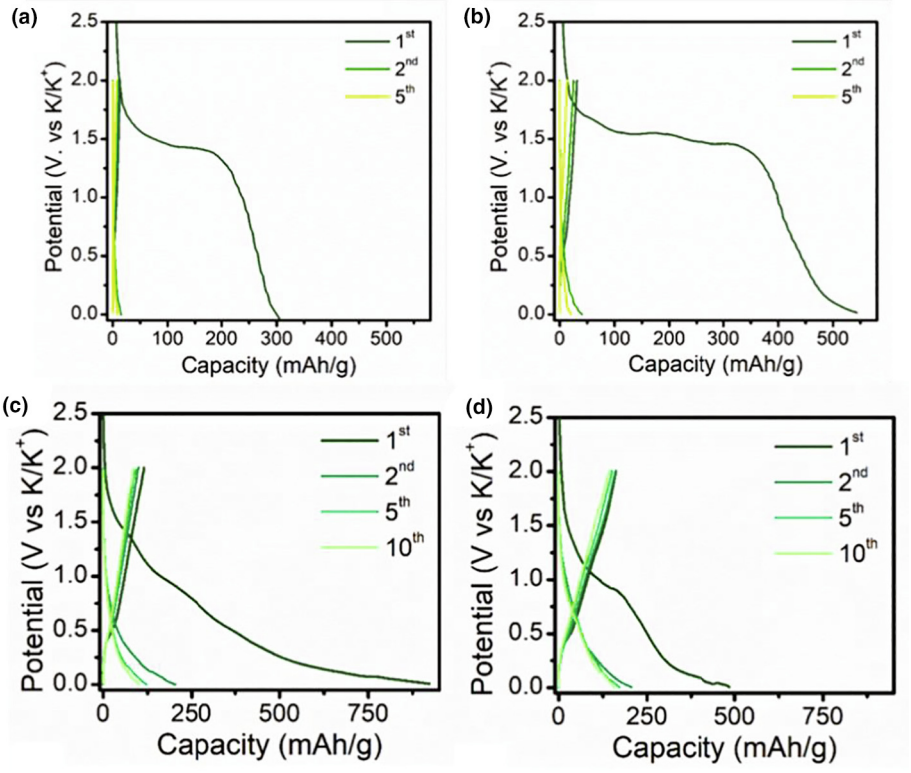

FIGURE 13

Galvanostatic curves for the germanane cycled at C/20 vs K using (a) 1 M KPF6 in 1:1 EC/DMC 1%FEC, (b) 1 M KFSI in 1:1 EC/DMC 1%FEC, (c) 0.8 M KPF6 in 1:1 EC/DEC, and (d) 0.8 M KFSI in 1:1 EC/DEC. Reproduced with permission [155]. © Wiley-VCH, 2020.

Please cite this article in press as: S. Imtiaz et al., Materials Today, (2021), https://doi.org/10.1016/j.mattod.2021.02.008

cal alloying of Pb by using micrometer Pb powder as the active material in 0.8 M KSFI in EC/DEC (1:1 by volume). The Pb electrode produced a reversible capacity of 105 mAh g^{-1}, in a modified charge/discharge process using a cut-off voltage of 0.0–0.8 V. The modified process was carried out by applying a high initial current pulse of 1 mV to the cell before the first discharge until the voltage reached 0.8 V. Increasing the potential above 0.8 V caused parasitic reactions which changed the reversible capacity. It was considered that this initial strong current pulse bypassed the catalytic surface reaction with the electrolyte, which hinders the alloying process. The charge/discharge profile of Pb showed three plateaus during discharge and two during charge. It was revealed by *ex-situ* and *operando* XRD analysis that potassiation of Pb followed the formation sequence of $K_{10}Pb_{48}$, K_4Pb_9 and KPb during the discharge, while only K_4Pb_9 was formed during the transition from KPb to Pb Fig. 14a and b. Nevertheless, because of its toxicity the literature on alloying of Pb in PIBs is extremely limited, however Pb is inexpensive and with proper packaging (e.g. in lead-acid batteries) the risk of toxicity could potentially be minimized.

In this section, we summarized the recent advances on group 14 and 15 based alloying-type anode materials that have been applied to PIBs so far. The reaction mechanisms of these alloying anode are discussed in detail, but there is still a lot of ambiguity on the specific alloying mechanism of some alloying anodes. Most of the work done in the literature has investigated the reaction mechanism by either *ex-situ* or *in-situ* XRD and it is difficult to characterize the minor phases by XRD. Therefore, the biggest challenge for alloying anodes is still to determine their accurate reaction mechanisms and to correlate phase evolutions. Although, we have discussed various strategies for the performance enhancement of alloying-type anodes, in-depth analysis to understand (1) structure stabilization during charge/discharge (2) irreversible side reactions and (3) capacity failure mechanisms requires significant consideration. Among various alloying anodes, Sb is the most sought anode in PIBs because of its potential to obtain high capacity. However, considering the large size of K, an improved electrode design is required to mitigate the volume expansion that causes capacity fade. Similarly for Bi, more advanced studies such as in-situ TEM/Raman, are required to understand its alloying behavior. Additionally, nanostructuring and electrolyte/binder optimizations are crucial to optimize performance of Bi anodes in PIBs. Section "Electrolytes and binders" will highlight the importance of electrolyte (salt, solvents) and binders on the performance of these alloying-type anodes. Based on the available data for Sn, it can be speculated that Sn cannot achieve similar importance for PIBs as it has gained in LIBs and SIBs, because of the one-electron reaction mechanism, leading to a limited capacity. However, the lower discharge plateau of Sn is favorable for anodes, and its bimetallic alloys with Sb and P can provide acceptable capacity. Even though P has the high theoretical capacity, it cannot accomplish the expectations in PIBs, which demands further detailed study to accurately determine the reaction mechanism and effective strategies to enhance K-storage capability. Si and Ge anodes have not shown convincing experimental results, but we believe that the complimentary knowledge from related studies with SIBs could assist to understand the obstacles. We have proposed some potential research directions for alloying-type anodes necessary for the development of practical PIBs in section 'Summary and perspective', which will open new avenues for advances needed for a commercially viable PIBs.

Electrolytes and binders

In previous sections we have discussed the alloying anodes for PIBs. However, recent studies showed that other than structural designs of alloying anodes, electrolyte engineering and salt chemistry are also crucial to enabling the high stability and capacity of alloying anodes. As already discussed, alloying anodes suffer from the huge volume expansion and contraction during potassiation/depotassiation processes that result in capacity fade and material pulverization. Electrolytes and salts play an important role in this regard as they can maintain a stable SEI layer which can avoid the pulverization of the anode and contribute to achieving a stable capacity. Among potassium salts, KPF_6 is the most explored, but it cannot dissolve completely into carbonate ester solvents leading to a white-colored suspension, which is possibly due to the low solvation energy for K^+ ions that limits the solubility of KPF_6 [17,201,202]. In contrast, KFSI is compatible in most of the electrolyte solvents, because it has higher solvation energy compared to KPF_6, and can effectively avoid excessive side reactions, suppress the growth of potassium dendrites and reduce polarization [149,203]. Komaba et al. [204] tested the solubility of KPF_6, KFSI, and other K-salts in PC, and

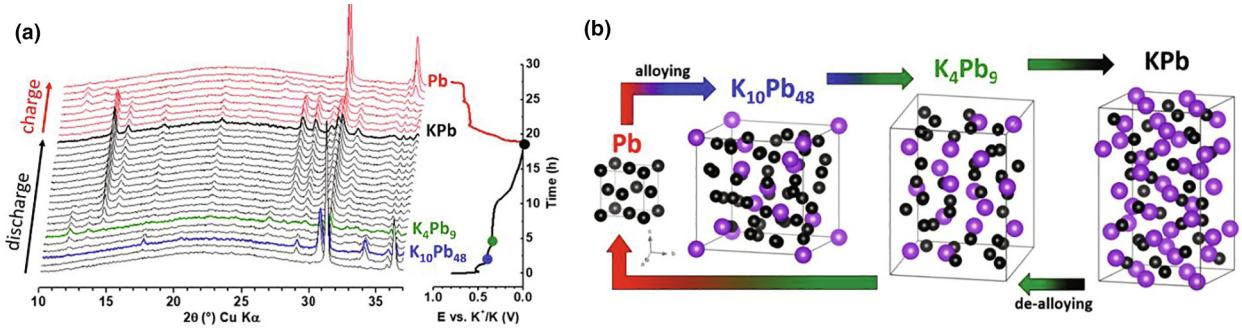

FIGURE 14

(a) *Operando* XRD measurement of the Pb during potassiation/depotassiation (left) with the corresponding voltage profile plotted as a function of time (right). Red and black pattern link to the charge and the discharge, respectively. (b) Scheme of the potassiation/depotassiation of the Pb electrode. Reproduced with permission [70]. © American Chemical Society, 2018.

Please cite this article in press as: S. Imtiaz et al., Materials Today, (2021), https://doi.org/10.1016/j.mattod.2021.02.008

observed higher conductivities of KFSI solutions than the KPF_6 -solutions in various solvents including EC/DEC, DME and PC indicating higher solubility of KFSI. Recently, KFSI appeared to be stable and displayed better CEs and capacity retentions for different alloying type anodes. Zhang et al. [106] observed significantly improved cycling stability of a Bi anode with KFSI salt in EC/DEC, which outperformed KPF_6. An abrupt capacity drop after only 4 cycles can be observed in Fig. 15a for Bi and Bi/RGO anodes in KPF_6 electrolytes, while the electrolyte with KFSI displayed stable cycling performance for both Bi and Bi/RGO. *Ex-situ* HRTEM showed that the SEI layer in the KFSI electrolyte was much more stable, as it maintained its integrity and displayed a similar thickness from the 2nd to 10th cycle. However, in the case of KPF_6, the SEI layer was found to be ruptured, and crevices were detected on its surface after only 5 cycles, leading to further irreversible decomposition of the electrolyte and growth of the new SEI layer (Fig. 15b–g). Furthermore, an XPS study of the SEI layer in the KPF_6 and KFSI electrolytes revealed that the SEI layer formed in KPF_6-based electrolytes was mainly from solvent-induced reduction, while the one in KFSI originated predominantly from salt reduction. Thus, the decomposition products of KFSI salts protected the electrolyte decomposition with the better cycling performance obtained because of the stable, uniform, and robust SEI. Sun and co-workers [107] demonstrated

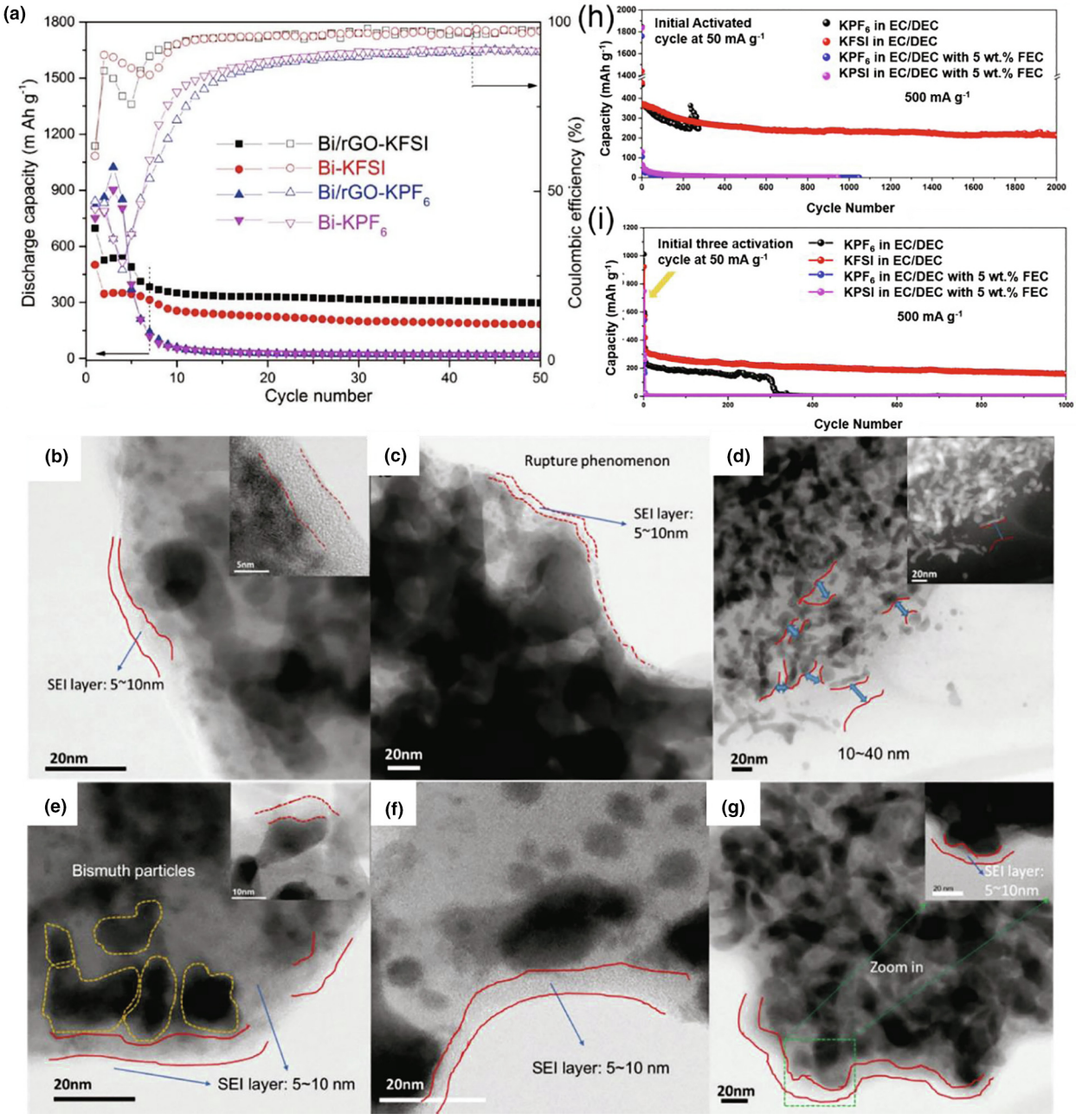

FIGURE 15

(a) Cycling performance and corresponding CE of Bi and Bi/RGO electrodes in KPF_6 and KFSI electrolytes at 50 mA g^{-1}. *Ex-situ* TEM images of Bi/rGO electrode after 2, 5, and 10 cycles in KFP_6 (b–d) and KFSI (e–g) electrolytes, with the insets showing higher magnification. Reproduced with permission [106] ©, Wiley-VCH. 2018. Cycling performance (h) GeP_5, (i) Sn_4P_3 with various electrolytes. Reproduced with permission. [149,154] ©, Elsevier 2018.

Please cite this article in press as: S. Imtiaz et al., Materials Today, (2021), https://doi.org/10.1016/j.mattod.2021.02.008

that a concentrated electrolyte (5 M KFSI instead of 1 M) approach significantly improved electrochemical storage performance because it effectively passivated the surface of the anode due to elevated reduction resistance.

Electrolyte additives are important and play an active part to improve the electrochemical performance of energy storage devices. Additives effectively assist the formation of a stable SEI layer, which prevents further electrolyte decomposition during cycling [205]. FEC has been adopted as an additive in electrolytes for PIBs, inspired by their successful application in SIBs [206]. FEC addition has been shown to improve the cycling performance and CE of Prussian blue analogue (PBA) cathodes [207,208]. Surprisingly, FEC addition has shown negative influence on anodes for PIBs and inferior cyclic behavior was observed by Bie et al. [209] and Lakshmi et al. [182] in their studies for graphite and SnS_2-rGO anodes, respectively. Guo's group also observed a fast capacity decay with 5 wt.% addition of FEC in both KPF_6 in EC/DEC and KFSI in EC/DEC electrolyte in different studies with GeP_5 [154] and Sn_4P_3 [149] anodes (Fig. 15h and i). It was observed that introduction of FEC increased the SEI layer and charge transfer resistance. In addition, potassium foil electrodes displayed higher hysteresis (±500 mV) in the electrolyte with FEC additive compared to without FEC (±200 mV), indicating large polarization due to the introduction of FEC [149]. Fourier transform infrared spectroscopy (FTIR) mapping proposed that the KFSI electrolyte without FEC formed a thin and uniform SEI layer on the GeP_5 anode, while addition of FEC led to the formation of an uneven SEI film, which results in low initial CE and poor cycling performance [154].

Solvents are a key component of electrolytes, and judicious selection of solvents can certainly boost the performance of PIBs. The commonly explored solvents for alloying-type anodes in PIBs are EC:DEC, EC:PC, PC, diethylene glycol dimethyl ether (diglyme) and DME. Huang et al. [105] experienced severe capacity decay with 1 M KPF_6 in EC/PC, showing a negligible capacity after 10 cycles. Whereas, a stable cycling performance was obtained with 1 M KPF_6 in diglyme, which produced a stable SEI on Bi anodes, and provided good structural stability of micro-sized Bi for long-term cycling. In another work, the electrochemical performance of Bi was studied in different electrolyte solvents such as EC/PC, PC, DME and diglyme with KPF_6, in which Bi showed good stability in DME and diglyme [103]. A Bi electrode tested with DME showed a porous network after cycling, whereas pulverization of particles occurred in PC-based electrolytes. The porous structure was beneficial for electrolyte penetration and contributed to the good cycling performance by accommodating large volume expansion. The porous structure was favored by the motion of surface Bi atoms *via* the strong chemical adsorption of DME molecules on the Bi. Other than the capacity and stability, DME based electrolytes have also been proved to be effective in improving initial CE [130]. Recently, Zhou et al. [210] systematically proved that a high capacity and stability can be attained in alloying anodes by just tuning the electrolyte composition. In their study, micro-Bi particles were employed with DME and PC solvents, which showed a high CE of 99.6%, and good capacity retention of 94.4% after 100 cycles in DME, whereas the capacity drastically decayed after only 5 cycles in PC. A new alloying reaction model was proposed which described that the surface of a pristine alloying anode can be classified in two sites, i.e., fresh and active sites (Fig. 16a and b). The fresh site will be stable when the electrolyte is compatible with the alloying anode, whereas it will be unstable in case of an incompatible electrolyte. An active site is a site on which the electrolyte can be decomposed because of high reactivity; thus, an SEI is formed on the anode surface. Based on this classification, in the compatible electrolyte, the electrolyte decomposition occurs only on the active sites to form the SEI during the first cycle; the fresh site remains stable, and more fresh sites are formed upon alloying anode pulverization during discharge. In contrast, in the case of incompatible electrolytes, the electrolyte decomposition occurs on both the active and fresh sites, giving rise to SEI coated active site, SEI-coated fresh site, and newly formed fresh site because of the alloying anode pulverization. As a result, a low CE was observed in the first cycle. In the subsequent cycles, the electrolyte decomposition continually occurred at the newly formed sites, resulting in severe capacity fading in incompatible electrolytes. These reports concluded that electrolyte has a great influence on the electrochemical performance of alloying type anodes and research efforts are needed to find more suitable electrolyte salts and solvents for alloying anodes in PIBs.

In addition to electrolyte, the choice of binders can significantly impact the preparation, mechanical robustness and electrochemical performance of the alloying-type anode materials for PIBs. Polymeric binders have been employed in the electrode preparation to enforce structural integrity and to promote cycle life and are considered a crucial component of the electrode. Some studies have found that suitable binders improve the CE and cycle life of anode materials for PIBs, but this data is mainly available for graphite based anodes [17,211–214]. To the best of our knowledge, at present, research on the influence of binder on the performance of alloying-type anode is limited to only a few reports. For example, Wu et al. [135] showed that sodium carboxymethyl cellulose (CMC) binder could improve the initial CE and cycling performance of P/C composite anodes due to the preformed SEI effect of CMC and avoidance of defluorination, as observed for polyvinylidene fluoride (PVDF). Glushenkov's group also observed an improved cycling stability of an Sb-C electrode by using biodegradable polymer gum arabic (GA) as a binder, compared to the conventional CMC. The GA gum was shown to enhance the binding force, improve the mechanical properties and withstand volume expansion stresses of the anode during potassiation/depotassiation [79]. Very recently, a noteworthy work was presented by Guo's group on the synergy of binders and electrolytes that enable high-capacity alloying anodes to maintain the electrode/interface stability against large volume changes [215]. By coupling the optimized binder, CMC and polyacrylic acid (PAA), with compatible electrolyte (3 M KFSI in DME) a high capacity of ~419 mAh g^{-1}, and a capacity retention of 84.3% after 600 cycles at 50 mA g^{-1} was obtained using microsized SnSb/C. This was attributed to the excellent mechanical properties of the CMC + PAA binder as investigated by nanoindentation and scratch tests. It showed much larger indentation depths and the highest reduced modulus and hardness compared to the other binders (CMC, CMC + styrene butadiene

Please cite this article in press as: S. Imtiaz et al., Materials Today, (2021), https://doi.org/10.1016/j.mattod.2021.02.008

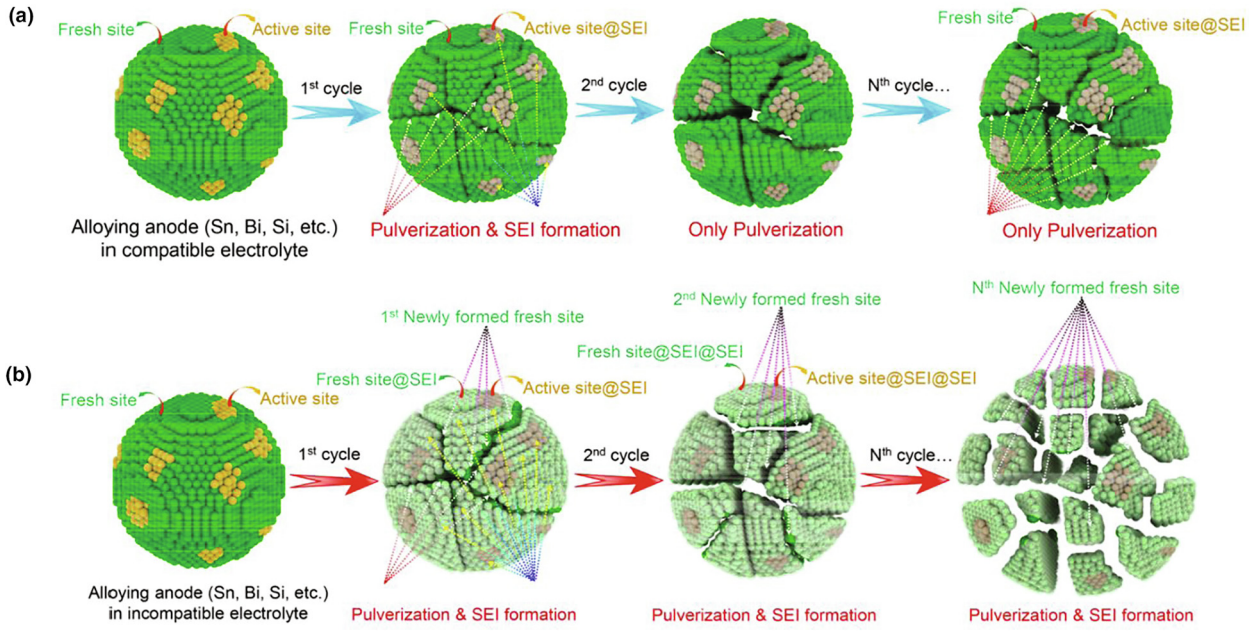

FIGURE 16

Alloying anode reaction model. Comparative behaviors in the (a) Compatible and (b) Incompatible electrolyte upon cycling. Reproduced with permission [210] © American Chemical Society, 2020.

rubber (SBR), CMC + cellulose acetate (CA)), and the stable SEI layers derived from the electrolyte. Thus, these studies highlight that the right choice of electrolyte and binder is critical to realizing high-performance anode in PIBs.

Apart from the alloying anodes, the understanding of K metal interfacial reaction with the electrolyte is also a key aspect to be explored. Considering the high chemical reactivity of K metal, the SEI layer formed is highly unstable, mainly due to the continuous interfacial reaction under huge volume variation during K plating/stripping [216,217]. These interfacial reactions affect the electrochemical performance of electrode materials against K metal in half-cells and have more serious effects in case of alloying-type anodes. Wang et al. [203] unveiled the impact of electrolyte chemistry on potassium metal by symmetric K/K cells and DFT calculations. The voltage curves and EIS spectra of symmetric cells was evaluated in different salts (KFSI and KPF_6, with EC/DEC), which showed stable cycling and constant impedance in the case of KFSI based electrolyte. Whereas, the low voltage hysteresis sharply decreased after a few cycles for KPF_6-based electrolyte, indicating a short circuit in the cell caused by K dendrites. DFT calculations showed that solvation energy of KFSI-based electrolytes is higher than that of KPF_6-related electrolytes, which leads to a higher degree of solvation molecules, reducing side reactions between potassium metal and electrolyte molecules. In addition, the lowest unoccupied molecular orbital energy of KFSI-EC/DEC complex was found to be lower than KPF_6-EC/DEC, implying a more reductive reactivity of KFSI species. Zhang et al. [149] also observed similar results with KFSI and KPF_6 based electrolytes, indicating that dendrite growth can be suppressed to some extent via reversible K metal plating/stripping, forming an even SEI layer. These results demonstrated that the proper selection of salt and solvent enable a strong and flexible SEI layer and support K^+ ion diffusion/desolvation for better K metal protection and cycling performance of alloying-type anodes. Nevertheless, the KFSI salt has shown improved cycling performance and stability in PIBs [88,112,155]. However, the FSI anion is corrosive for aluminum foil under anodic polarization (>4.0 V vs. K/K^+), which may hinder its application for high-voltage cathodes [201,218].

Summary and perspective

This review summarizes the research progress of alloying-type anodes from group 14 and 15 for PIBs. This class of alloying-type anodes provides high theoretical capacities, yet the biggest challenge is to mitigate the huge volume expansion upon cycling. This review discusses various strategies for the performance enhancement of alloying-type anodes, including nanostructure design, suitable additives (combining carbonaceous materials, relevant oxides and sulfides materials that store K with alloying-conversion reaction), and the important influence of electrolyte salts and solvents compatibility. Although achieving practical PIBs in real-world energy storage systems is still a long way off, significant progress has been accomplished in terms of high capacity and durability for these alloying-type anodes. Here, we summarize the potential research directions for alloying-type anodes necessary for the development of practical PIBs.

(1) *Nanostructure design of alloying anodes:* Nanostructure engineering has a multitude of advantages as outlined in previous sections, although there is considerable scope for this research to be extended. For instance, a better focus on nanostructure optimization in terms of size control (diameter and length), density/areal loading, interconnected networks, and their formation by cost effective and scalable synthesis strategies. The optimum results will be

Please cite this article in press as: S. Imtiaz et al., Materials Today, (2021), https://doi.org/10.1016/j.mattod.2021.02.008

obtained where the anode is effectively designed to address fundamental issues, including (*i*) electrode swelling, which is affected by the huge intrinsic volumetric change of anode materials (e.g., Sb ~407% and Bi ~400%), is crucial to the cycling performance, volumetric energy density and battery safety. This can be addressed at both the individual particles or nanowires (NWs) level by a design-to-prevent pulverization/cracking strategy, and at the electrode level to ensure a balanced distribution of voids and active elements which is important for the electrode swelling management, (*ii*) capacity fading should be mitigated to ensure efficient cell capacity retention during long cycling by ensuring a balanced and minimal trade-off between robust electrode structures, capacity, and stable electrolytes to inhibit or circumvent any detrimental side-reactions during cycling. This can potentially be achieved by rationally designing complex electrode structures (e.g., heterostructures, carbon-sheathing, etc.) as they can offer more choices for optimizing anode structure (e.g., to alleviate stresses during cycling) or tuning the electrochemical behavior and overall battery performance. Thus, we propose NW-based anode engineering as NWs have the advantages of being directly grown on the current collector, which can facilitate efficient electrical transport, and shortened the ion diffusion length and have the potential to boost rate performance. This is an attractive route to allow additive and binder-free electrodes in contrast to composite nanoparticle based electrodes widely reported in the literature.

(2) *Low-crystalline and amorphous metals:* The common theme in the summarized works in this review is that crystalline electrodes possess a low discharge plateau in the first cycle, but the plateau gradually increases in the subsequent cycles. This indicates the kinetic difficulty of K^+ diffusion in the initial potassiation process, which can be eased in subsequent cycles. Furthermore, many cases have shown that the degree of crystallinity of the alloying element is greatly lowered with prolonged cycles, which in turn greatly releases structural strain, reduces ion diffusion energy barrier or even generates new diffusion pathways. As a result, it is reasonable to speculate that an initially low crystallinity or even amorphization of the alloying element could potentially realize the afore-mentioned advantages at the start of the potassiation process. Therefore, it is worth investigating the synthetic methods to obtain active alloying elements in a form with a low degree of crystallinity and systematically investigating their K-storage mechanism in comparison to their crystalline counterparts. Research toward amorphous structures which, in the case of Si, have exhibited significantly improved electrochemical performance than crystalline counterparts because the amorphous structures offer higher potential which can allow an increase of the cut-off voltage and inhibit dendrite formation, thereby, improving battery safety. Furthermore, amorphous structures provide a good tolerance to intrinsic stress/strain effects, thereby enhancing fracture resistance and improving cell cycle life. Off course there are trade-offs, but the numerous advantages of amorphous materials are worth exploring for PIB systems which is currently lacking in the literature and, therefore, more research is needed to reach a reliable conclusion. Indeed, various research in LIB systems showed that the decrease of energy density in full cells based on amorphous materials is minimal and remains advantageous compared to the abrupt capacity failures that are intrinsic characteristic of crystalline counterparts. Furthermore, the possibility to increase the cut-off voltage would be beneficial for inhibiting K-dendrite formation which is very important for enhancing battery life and safety.

(3) *Binary and ternary alloys:* despite the high theoretical capacities that some of the group 14 and 15 metals have, the stoichiometries that the theoretical capacities are based on have by far not been electrochemically reached. Some metals (e.g., Bi) have a high compositional tolerance towards K but at the same time exhibit high volumetric expansion behavior. Other metals (e.g., Sn) exhibits an acceptable level of volume change but display a relatively high discharge plateau. An important finding that clearly emerges from previous works on PIBs is that alloys often outperform their constituent metals. The binary/ternary alloys could give rise to the emergence of new properties that are absent in the individual elements. In addition, the different alloying potential of binary/ternary alloys can lead to separated reaction processes that act as buffer matrices to better accommodate volume variations and avoid the abrupt simultaneous expansion/contraction of the electrode. Despite the low capacity of Sn, it has proven to be very effective for K-storage when combined with P [149,219], because it can to provide stability and high conductivity in Sn-P alloys, thus the issue of low electronic conductivity (1×10^{-10} S cm^{-1}) and a large volume expansion of P can be addressed [148,220]. There is a wide compositional range for binary systems (e.g., Bi-Sb and Sn-Sb) and ternary systems (e.g., Sn-Bi-Sb) for anode design. The freedom of adjusting the compositions of alloys could open a new avenue for designing electrodes that can efficiently store K-ions and allow detailed insights into the storage mechanism. While group 14 and 15 elements are the most studied materials currently, it may be worth investigating potentially active and abundant metallic materials and their composite assemblies with intercalation type materials such as layered oxides, polyanionic and metal hexacyanometalates. There is a huge window of opportunity to pursue a wide range of candidate alloys as well as intermetallics in this regard.

(4) *Cell optimization:* one of the major attractiveness of alloying anodes is the high theoretical capacities. It is worth emphasizing that when designing a full cell, a high anode capacity (gravimetric) needs an increase of cathode mass to balance the charge, given that a high anode capacity does not necessarily contribute to an increase of the full-cell capacity. Studies of LIBs have shown that full-cell gravimetric capacity and energy density run into a saturated state for anode capacities beyond 1000 mAh g^{-1}, when the cathode capacity is 200 mAh g^{-1} or less [221]. Currently, the best performing PIB cathode chemistries are

Please cite this article in press as: S. Imtiaz et al., Materials Today, (2021), https://doi.org/10.1016/j.mattod.2021.02.008

KFeFe-PBA and KMnFe-PBA with capacities in the range of 130–142 mAh g^{-1} [209,222,223]. Therefore, a high anode capacity would generate a gain in full-cell capacity and energy density only if a high capacity cathode would be deployed [224]. In this context, alloying anodes should be carefully designed to deliver an optimized capacity and hence maximize their contribution to the full-cell capacity and energy density relative to the enhanced cathode capacity. Thus, for a linear increase of the cell capacity/energy density of practical PIBs, higher capacity cathode chemistries must be developed to complement the high capacity alloying-type anodes in order to prevent dilution of the capacity gains of the anodes.

For the practical implementation of the group 14 and 15 based anodes in high-energy PIBs, it is also essential to critically investigate the electrochemical behavior and electrode swelling characteristics in a full-cell configuration, which is rarely investigated in the literature. Also lacking at present is the data on the influence of binders on the performance of alloying anodes, both in half-cells and full-cells. We believe a comprehensive design of the electrochemical cells with the aim of high volumetric energy density, based on high capacity anode/cathodes, will lay a good foundation toward the realization of high-energy PIBs utilizing these group 14 and 15 based electrodes.

(5) *Unclear electrochemical behaviors:* despite the significant progress made in understanding the reaction mechanisms of alloying anodes with K, the detailed potassiation/depotassiation mechanism of some key alloying materials is still not fully understood and thus under debate, particularly for Si, Ge, and P. Consequently, in-depth understanding via advanced characterization tools are needed to reliably record the electrochemical alloying processes. Besides the *operando* XRD studies commonly reported in the literature, further deployment of more advanced nanoscale tools such as *in-situ* scattering (pair distribution function (PDF), neutron diffractions (NDs)), *in-situ* microscopy (TEM and atomic force microscopy (AFM)), *in-situ* spectroscopy (FTIR, Raman, X-ray absorption spectroscopy (XAS), nuclear magnetic resonance (NMR)) are highly recommended for in-depth analysis and understanding of the structural behavior of the electrodes in response to the potassiation/depotassiation, the impact of electrolyte chemistry, and the K-trapping mechanisms involved in the dynamic electrochemical processes. In addition, these techniques can also provide deeper analysis of the surface/interface, bulk structure and morphology, and the microstructure relationship of the electrode. These activities should possibly be complemented by theoretical analysis/computations (e.g., DFT, MD simulations) to reliably predict and/or provide a clear and accurate representation of the electrode kinetics during K reaction, and the effects of alloying elements and/or electrolyte additives. This will effectively guide the rational design of efficient electrodes toward high performance PIBs, and provide a better understanding of the specific alloying mechanisms, interface chemistry, probable failure mechanisms, and ultimately offer valuable guiding principles not only for designing efficient and reliable electrodes but also in search of suitable new materials and electrolytes for advanced PIBs.

(6) *Electrolyte and binder optimization:* the compatibility and stability of electrolyte salts and solvents are also crucial factors that can significantly impact the electrochemical performance of alloying-type anode materials for PIBs. Many studies found KFSI salt to be more stable than KPF_6, providing good CEs and capacity retention; however, it may not be suitable for high voltage cathodes. In addition, the use of conventional electrolyte additives such as FEC appears not suitable for PIBs. Thus, in order to improve the electrochemical performance of alloying-type anode materials, it is imperative for research efforts to be devoted to electrolyte optimization, including salts, solvents, and additives. Other than the organic solvents, ionic liquids (ILs) are also promising category of electrolytes because of their higher ionic conductivity, effective SEI, higher operational safety, and wider electrochemical stability windows. For example, Pasta's group recently demonstrated the cycling of potassium manganese hexacyanoferrate (KMF) cathode and a graphite anode using a KFSI in $Pyr_{1,3}FSI$ ILs electrolyte up to 4.3 V (versus K^+/K) with high CE and minimal corrosion effects on the Al current collector [225]. In addition, Onuma et al. demonstrated a K-ion battery of graphite//$K_2Mn[Fe(CN)_6]$ configuration with an ILs electrolyte which exhibited significantly improved redox performance compared to conventional KPF_6 carbonate ester solution [226]. Accordingly, ILs could be a potential electrolyte in alloying-type anodes and could address the issues of low CE and compatibility with high voltage cathodes while also addressing the challenges associated with the larger size K^+ uptake. Therefore, formulating and trialing new electrolytes or optimizing present ones must take new chemistries and molecular structures into consideration such as ILs and additives, and be directed at achieving electrolytes with high ionic conductivity and stability for the efficient transport of the large sized K^+, while inhibiting any harmful side reactions and promoting a stable SEI layer formation and superior CE.

There is also the need to understand the dendrite issue that occurs with highly reactive K metal. The uncontrollable interfacial reactions with the electrolyte, and huge volume change of K metal leads to the continuous SEI breakage and reformation on the dendrite structure, which results in a low CE and a rise in impedance [217]. It is to be noted that previously developed fluorinated solvents are nearly inert in PIBs. Thus, development of suitable additives is urgently required. Moreover, the SEI formed on K metal even with KFSI salt and carbonate electrolytes is still far from stable, thus an alternative strategy of introducing an artificial barrier [227–229] between the metal and the electrolyte is an important future focus area for PIB research.

Additionally, the choice of binder is also vital to overcome the challenge of low initial CE of alloying-type anode. For example, Komaba et al. studied the effect of different binders (CMC, PANa and PVDF) on initial CE for graphite anodes and found superior initial CE of 89% and 79% with CMC and PANa, respectively,

Please cite this article in press as: S. Imtiaz et al., Materials Today, (2021), https://doi.org/10.1016/j.mattod.2021.02.008

compared to only 59% with PVDF [17]. This improvement of initial CE with CMC and PANa was attributed to the preformed SEI effect as well as the avoidance of defluorination, as observed for PVDF. This kind of analysis is still lacking for alloying-type anodes and there is an opportunity to conduct similar studies by formulating new or optimized binders to get more practical alloying-type anodes for PIBs.

In conclusion, the abundant resources and high energy density of PIBs make it certainly a promising candidate for beyond LIBs particularly for large scale EESSs. While alloying-type anodes offer great opportunities, realizing high performance and long cycle life PIB using these electrodes requires persistent and continued efforts to design suitable and robust anode structures, generate optimal formulations and electrolyte chemistries and carry out full cell studies with *in-situ* and *operando* investigations to decipher all mechanistic pathways. The substantial progress achieved to date from a relatively small number of groups, as highlighted in this review, shows that an even greater research focus on these topics from the wider materials and battery research communities can deliver the confluence of advances needed for a commercially viable PIB.

Declaration of Competing Interest

The authors declare that they have no known competing financial interests or personal relationships that could have appeared to influence the work reported in this paper.

Acknowledgements

K.M.R. acknowledges Science Foundation Ireland (SFI) under the Principal Investigator Program under contract nos. 16/IA/4629 and under grant no. SFI 16/M-ERA/3419 and European Union's Horizon 2020 Research and Innovation Program under grant agreement no. 814464 (Si-DRIVE) project. K.M.R further acknowledges IRCLA/2017/285 and SFI Research Centers MaREI, AMBER and CONFIRM 12/RC/2278_P2, 12/RC/2302_P2, and 16/RC/3918.

References

[1] T. Hosaka et al., Chem. Rev. 120 (14) (2020) 6358.
[2] M. Li et al., Nat. Rev. Mater 5 (4) (2020) 276.
[3] J. Liu et al., Chem. Soc. Rev. 49 (6) (2020) 1624.
[4] Y. Wu et al., Energy Storage Mater. 34 (2021) 483.
[5] Y. Gao et al., ChemElectroChem 6 (17) (2019) 4689.
[6] X. Zhang et al., Electrochem. Energy Rev. 2 (1) (2018) 29.
[7] Z.A. Zafar et al., J. Mater. Chem. A 5 (12) (2017) 5646.
[8] M. Sha et al., Energy Environ. Mater. 3 (1) (2020) 56.
[9] S. Zhang et al., Mater. Today 39 (2020) 9.
[10] S.-S. Fan et al., J. Materiomics 6 (2) (2020) 431.
[11] Y.-S. Xu et al., J. Mater. Chem. A 7 (9) (2019) 4334.
[12] X. Zhang et al., Adv. Energy Mater. 10 (22) (2020) 1904118.
[13] W. Ren et al., Nano Lett. 17 (8) (2017) 4713.
[14] J. Chen et al., Small Methods 4 (1) (2019) 1900648.
[15] J. Xie et al., Mater. Today Adv. 6 (2020) 100035.
[16] Y. Wu et al., Adv. Mater. 31 (50) (2019) e1901414.
[17] S. Komaba et al., Electrochem. Commun. 60 (2015) 172.
[18] X. Zhang et al., Curr. Opin. Electrochem. 18 (2019) 24.
[19] Z. Liu et al., Energy Storage Mater. 34 (2021) 211.
[20] H. Kim et al., Trends Chem. 1 (7) (2019) 682.
[21] Q. Zhang et al., Electrochem. Energy Rev. 1 (4) (2018) 625.
[22] W. Zhang et al., Sci. Adv. 5 (5) (2019) eaav7412.
[23] Y. Wang et al., Energy Storage Mater. 34 (2021) 436.
[24] C. Vaalma et al., Nat. Rev. Mater 3 (2018) 4.
[25] C. Vaalma et al., Curr. Opin. Electrochem. 9 (2018) 41.
[26] K. Kubota et al., Chem. Rec. 18 (4) (2018) 459.
[27] T.A. Pham et al., J. Phys. Chem. C 121 (40) (2017) 21913.
[28] R.A. Adams et al., J. Power Sources 375 (2018) 131.
[29] R. Rajagopalan et al., Adv. Funct. Mater. 30 (12) (2020) 1909486.
[30] V. Gabaudan et al., Front. Energy Res. (2019) 7, https://doi.org/10.3389/fenrg.2019.00046.
[31] X. Wu et al., Adv. Energy Mater. 9 (21) (2019) 1900343.
[32] J. Ge et al., Adv. Energy Mater. 10 (4) (2019) 1903277.
[33] Y. Wu et al., Nano Res. 12 (12) (2019) 2997.
[34] K. Cao et al., J. Electroanal. Chem. 841 (2019) 51.
[35] Y. Liu et al., Energy Storage Mater. 22 (2019) 66.
[36] J. Zhou et al., InfoMat 2 (3) (2020) 437.
[37] C. Wang et al., Chem. Commun. 55 (12) (2019) 1801.
[38] Q. Zhang et al., Chem. Eur. J. (2020), https://doi.org/10.1002/chem.202005259.
[39] Q. Xue et al., J. Mater. Chem. A 6 (26) (2018) 12559.
[40] C. Zhang et al., ACS nano 13 (1) (2019) 745.
[41] L. Chen et al., Electrochim. Acta 294 (2019) 46.
[42] Q. Deng et al., Nano Energy 33 (2017) 350.
[43] T. Kennedy et al., ACS Nano 9 (7) (2015) 7456.
[44] I.S. Aminu et al., Adv. Funct. Mater. 30 (38) (2020) 2003278.
[45] H. Liu et al., ACS Mater. Lett. 1 (2) (2019) 217.
[46] M.N. Obrovac et al., Chem. Rev. 114 (23) (2014) 11444.
[47] C.M. Park et al., Chem. Soc. Rev. 39 (8) (2010) 3115.
[48] K.-X. Lei et al., Rare Met. 39 (9) (2020) 989.
[49] Z. Jian et al., J. Am. Chem. Soc. 137 (36) (2015) 11566.
[50] M. Chen et al., Energy Storage Mater. 19 (2019) 163.
[51] Y. Fang et al., Adv. Mater. (2020) 2002976.
[52] S. Xu et al., J. Mater. Chem. A 8 (31) (2020) 15547.
[53] M. Sha et al., Carbon Energy 2 (3) (2020) 350.
[54] M. Lao et al., Adv. Mater. 29 (48) (2017) 1700622.
[55] J. Niu et al., Adv. Energy Mater. (2020) 2000697.
[56] H. Zhang et al., Adv. Energy Mater. 8 (17) (2018) 1702582.
[57] I. Sultana et al., Adv. Funct. Mater. 28 (5) (2018) 1703857.
[58] Y. Xu et al., Chem. Asian J. 15 (11) (2020) 1648.
[59] K. Song et al., Small 15 (2019) 1903194.
[60] J.-Y. Hwang et al., Adv. Funct. Mater. 28 (43) (2018) 1802938.
[61] H. Kim et al., Adv. Energy Mater. 7 (17) (2017) 1700098.
[62] L.C. Loaiza et al., Small 16 (5) (2020) e1905260.
[63] S. Lee et al., J. Power Sources 415 (2019) 119.
[64] Q. Yang et al., Electrochem. Commun. 101 (2019) 68.
[65] Q. Wang et al., J. Phys. Chem. C 121 (23) (2017) 12652.
[66] W.D. McCulloch et al., ACS Appl. Mater. Interfaces 7 (47) (2015) 26158.
[67] V. Gabaudan et al., J. Phys. Chem. C 122 (32) (2018) 18266.
[68] X. Huang et al., J. Mater. Chem. A 8 (16) (2020) 7641.
[69] I. Sultana et al., J. Mater. Chem. A 5 (45) (2017) 23506.
[70] V. Gabaudan et al., ACS omega 3 (9) (2018) 12195.
[71] H. Gao et al., EcoMat 2 (2) (2020) e12027.
[72] H. Tan et al., Adv. Funct. Mater. 29 (14) (2019) 1808745.
[73] J. Sangster et al., J. Phase Equilibria 14 (4) (1993) 510.
[74] J. Zheng et al., Energy Environ. Sci. 12 (2) (2019) 615.
[75] C. Han et al., Nanoscale 10 (15) (2018) 6820.
[76] Z. Yi et al., Nanoscale 10 (27) (2018) 13236.
[77] N. Cheng et al., Chem. Commun. 55 (83) (2019) 12511.
[78] X. Ge et al., Angew. Chem. Int. Ed. Engl. 58 (41) (2019) 14578.
[79] I. Sultana et al., J. Power Sources 413 (2019) 476.
[80] S. Liu et al., Energy Environ. Sci. 9 (4) (2016) 1229.
[81] Y. An et al., ACS nano 12 (12) (2018) 12932.
[82] X. Yang et al., Chem. Eur. J. 26 (26) (2020) 5818.
[83] H. Wang et al., Mater. Res. Bull. 103 (2018) 32.
[84] Y. Han et al., Energy Storage Mater. 20 (2019) 46.
[85] Q. Liu et al., Chem. Commun. 54 (83) (2018) 11773.
[86] Y.-H. Zhu et al., Joule 2 (4) (2018) 736.
[87] T. Kennedy et al., Adv. Mater. 28 (27) (2016) 5696.
[88] K. Cao et al., Adv. Mater. Technol. 5 (6) (2020) 2000199.
[89] H. Yang et al., Nano Lett. 20 (1) (2020) 758.
[90] A.M. Tripathi et al., Chem. Soc. Rev. 47 (3) (2018) 736.
[91] J. Yang et al., Chem. Soc. Rev. 45 (20) (2016) 5717.
[92] N. Liu et al., Nat. Nanotechnol. 9 (3) (2014) 187.
[93] Y. Wu et al., Chem 4 (3) (2018) 438.
[94] H. Huang et al., Angew. Chem. Int. Ed. Engl. 59 (34) (2020) 14504.
[95] Z. Yi et al., J. Mater. Chem. A 7 (19) (2019) 12283.
[96] J. Zhou et al., Adv. Mater. 29 (35) (2017) 1702061.

Please cite this article in press as: S. Imtiaz et al., Materials Today, (2021), https://doi.org/10.1016/j.mattod.2021.02.008

[97] Y. Lu et al., Sci. China Chem. 60 (12) (2017) 1533.
[98] Y. Liu et al., Nat. Commun. 9 (1) (2018) 3645.
[99] V. Lakshmi et al., J. Mater. Chem. A 8 (22) (2020) 11424.
[100] Y. Shi et al., Nanomaterials 9 (4) (2019) 560.
[101] H. Yang et al., Adv. Funct. Mater. 29 (13) (2019) 1809195.
[102] A. Wang et al., Small (2020) 2004022.
[103] K. Lei et al., Angew. Chem. Int. Ed. Engl. 57 (17) (2018) 4687.
[104] A. Petric et al., J. Phys. F: Met. Phys. 18 (7) (1988) 1473.
[105] J. Huang et al., Adv. Energy Mater. 8 (19) (2018) 1703496.
[106] Q. Zhang et al., Adv. Energy Mater. 8 (15) (2018) 1703288.
[107] R. Zhang et al., Chem. Sci. 9 (29) (2018) 6193.
[108] X. Wu et al., Adv. Funct. Mater. (2020) 2003838.
[109] H. Gao et al., J. Power Sources 379 (2018) 1.
[110] X. Cheng et al., J. Mater. Chem. A 7 (9) (2019) 4913.
[111] S. Qi et al., Phys. Status Solidi Rapid Res. Lett. 13 (10) (2019) 1900209.
[112] F. Xie et al., Matter 1 (6) (2019) 1681.
[113] T. Jiao et al., J. Mater. Chem. A 8 (17) (2020) 8440.
[114] K.T. Chen et al., ACS Nano 14 (9) (2020) 11648.
[115] V. Gabaudan et al., J. Mater. Chem. A 7 (25) (2019) 15262.
[116] H. Xie et al., J. Mater. Chem. A 5 (20) (2017) 9661.
[117] P. Xiong et al., ACS Nano 14 (1) (2020) 1018.
[118] J. Wang et al., ACS Nano 13 (3) (2019) 3703.
[119] J.O. Besenhard et al., Solid State Ion. 40–41 (1990) 525.
[120] Z. Li et al., Acc. Chem. Res. 48 (6) (2015) 1657.
[121] F. Xin et al., Electrochem. Energy Rev. 3 (4) (2020) 643.
[122] J. Sangster et al., J. Phase Equilibria Diffus. 19 (1) (1998) 67.
[123] H. Kim et al., Adv. Energy Mater. 8 (9) (2018) 1702384.
[124] I. Sultana et al., Chem. Commun. 52 (59) (2016) 9279.
[125] T. Ramireddy et al., J. Electrochem. Soc. 164 (12) (2017) A2360.
[126] K. Huang et al., J. Mater. Chem. A 6 (2) (2018) 434.
[127] Y. Yang et al., Mater. Lett. 256 (2019) 126613.
[128] H. Wang et al., Appl. Mater. Today 15 (2019) 58.
[129] M. Shimizu et al., ACS Appl. Energy Mater. 1 (12) (2018) 6865.
[130] Z. Wang et al., J. Mater. Chem. A 7 (23) (2019) 14309.
[131] J. Li et al., ACS Appl. Mater. Interfaces 12 (4) (2020) 4414.
[132] D. Yang et al., Nanoscale 11 (33) (2019) 15402.
[133] J.M. Sangster, J. Phase Equilibria Diffus. 31 (1) (2009) 68.
[134] W. Zhang et al., J. Am. Chem. Soc. 139 (9) (2017) 3316.
[135] X. Wu et al., J. Power Sources 378 (2018) 460.
[136] R. Gusmao et al., Angew. Chem. Int. Ed. Engl. 56 (28) (2017) 8052.
[137] Y. Sui et al., Mater. Today (2020), https://doi.org/10.1016/j.mattod.2020.09.005.
[138] Y. Fu et al., Adv. Energy Mater. 8 (13) (2018) 1703058.
[139] P. Xiong et al., Small (2018) e1802140.
[140] I. Sultana et al., J. Mater. Chem. A 7 (5) (2019) 2421.
[141] Y. Wu et al., Nano. Lett. 19 (2) (2019) 1351.
[142] M. Batmunkh et al., Adv. Mater. 28 (39) (2016) 8586.
[143] W. Li et al., Nano Lett. 15 (3) (2015) 1691.
[144] Y. Tao et al., Appl. Mater. Today 15 (2019) 18.
[145] X. Wu et al., J. Mater. Chem. A 8 (25) (2020) 12705.
[146] R. Jain et al., ACS Nano 13 (12) (2019) 14094.
[147] W. Yang et al., Ionics 25 (10) (2019) 4795.
[148] X. Zhao et al., Chem. Eng. J. 370 (2019) 677.
[149] W. Zhang et al., Joule 2 (8) (2018) 1534.
[150] X.-T. Zheng et al., ACS Sustain. Chem. Eng. 8 (50) (2020) 18535.
[151] K. Stokes et al., ACS Nano 11 (10) (2017) 10088.
[152] T. Kennedy et al., Nano Lett. 14 (2) (2014) 716.
[153] K. Stokes et al., Nano Lett. 18 (9) (2018) 5569.
[154] W. Zhang et al., Nano Energy 53 (2018) 967.
[155] L.C. Loaiza et al., Batteries Supercaps. 3 (5) (2020) 417.
[156] B. Ji et al., Adv. Mater. 29 (19) (2017) 1700519.
[157] Z. Huang et al., Solid State Ion. 324 (2018) 267.
[158] L. Wang et al., J. Appl. Electrochem. 48 (10) (2018) 1115.
[159] X.-D. He et al., J. Mater. Chem. A 7 (16) (2019) 9629.
[160] Y.N. Ko et al., ACS Appl. Mater. Interfaces 11 (31) (2019) 27973.
[161] Q. Liu et al., Energy Technol. 7 (10) (2019) 1900634.
[162] W. Luo et al., Nano Res. 12 (5) (2019) 1025.
[163] S. Wang et al., Adv. Funct. Mater. (2020) 2001588.
[164] L. Yang et al., Chem. Eng. J. 385 (2020) 123838.
[165] Y. Zhang et al., Appl. Surf. Sci. 499 (2020) 143907.
[166] Y. Zhao et al., Small 16 (2) (2020) e1905789.
[167] H. Li et al., Nanoscale 12 (7) (2020) 4309.
[168] S. Su et al., ACS Appl. Mater. Interfaces 11 (25) (2019) 22474.
[169] X. Xiang et al., Appl. Surf. Sci. 514 (2020) 145947.
[170] L. Zeng et al., Sci. China Mater. 63 (10) (2020) 1920.
[171] C. Shen et al., J. Mater. Chem. A 8 (1) (2020) 453.
[172] W. Li et al., Chem. Commun. 55 (46) (2019) 6507.
[173] J. Hu et al., Nano Res. 13 (10) (2020) 2650.
[174] J. Wang et al., Adv. Energy Mater. (2020) 2000884.
[175] G. Suo et al., J. Electroanal. Chem. 833 (2019) 113.
[176] H. Qiu et al., Energy Environ. Sci. 13 (2) (2020) 571.
[177] Z. Huang et al., Mater. Lett. 219 (2018) 19.
[178] Z. Huang et al., Nanotechnology 29 (37) (2018) 375702.
[179] Z. Wang et al., J. Power Sources 441 (2019) 227191.
[180] Z. Chen et al., Small 14 (17) (2018) e1703818.
[181] G. Suo et al., J. Mater. Sci. Technol. 55 (2020) 167.
[182] V. Lakshmi et al., Chem. Commun. 53 (59) (2017) 8272.
[183] D.-S. Bin et al., Nano Energy 60 (2019) 912.
[184] L. Fang et al., Small (2019) 1804806.
[185] D. Li et al., ChemSusChem 12 (12) (2019) 2689.
[186] C. Sheng et al., Batteries Supercaps. 3 (1) (2019) 56.
[187] K. Cao et al., Chem. Eng. J. 406 (2021) 126902.
[188] X. Huang et al., ACS Sustain. Chem. Eng. 6 (12) (2018) 16308.
[189] D. Liu et al., Nano Energy 52 (2018) 1.
[190] H. Wang et al., Chem. Eur. J. 24 (52) (2018) 13897.
[191] W.C. Chang et al., Adv. Sci. 6 (9) (2019) 1801354.
[192] K. Fang et al., Nano Energy 69 (2020) 104451.
[193] H. Jin et al., Angew. Chem. Int. Ed. Engl. 59 (6) (2020) 2318.
[194] W. Li et al., ACS Appl. Mater. Interfaces 11 (25) (2019) 22364.
[195] X. Wang et al., J. Alloys Compd. 821 (2020) 153268.
[196] Q. Tan et al., J. Mater. Chem. A 7 (26) (2019) 15673.
[197] X. Chen et al., ACS Energy Lett. 4 (7) (2019) 1496.
[198] Z. Yi et al., Small 16 (2) (2020) e1905301.
[199] B. Li et al., Small 16 (6) (2020) e1906595.
[200] C. Lin et al., J. Power Sources 443 (2019) 227276.
[201] J. Zhang et al., Nano Energy 60 (2019) 340.
[202] Y. Liu et al., Small 16 (44) (2020) e2004096.
[203] H. Wang et al., Angew. Chem. Int. Ed. Engl. 58 (46) (2019) 16451.
[204] T. Hosaka et al., Chem. Commun. 54 (60) (2018) 8387.
[205] T. Kennedy et al., J. Power Sources 359 (2017) 601.
[206] M.D. Slater et al., Adv. Funct. Mater. 23 (8) (2013) 947.
[207] G. He et al., ACS Energy Lett. 2 (5) (2017) 1122.
[208] M. Qin et al., ACS Sustain. Chem. Eng. 7 (13) (2019) 11564.
[209] X. Bie et al., J. Mater. Chem. A 5 (9) (2017) 4325.
[210] L. Zhou et al., ACS Energy Lett. 5 (3) (2020) 766.
[211] X. Wu et al., Ionics 25 (6) (2018) 2563.
[212] J. Li et al., ACS Appl. Mater. Interfaces 11 (17) (2019) 15581.
[213] X. Zou et al., Phys. Chem. Chem. Phys. 19 (39) (2017) 26495.
[214] J. Zhao et al., Adv. Funct. Mater. 26 (44) (2016) 8103.
[215] J. Wu et al., Nano Energy 77 (2020) 105118.
[216] M. Zhou et al., Adv. Mater. (2021) 2003741.
[217] H. Wang et al., Energy Environ. Sci. 13 (12) (2020) 4583.
[218] E. Cho et al., Electrochem. Commun. 22 (2012) 1.
[219] D. Li et al., Energy Storage Mater. 23 (2019) 367.
[220] B. Li et al., Carbon 168 (2020) 468.
[221] T. Placke et al., J. Solid State Electrochem. 21 (7) (2017) 1939.
[222] S. Dhir et al., Chem 6 (10) (2020) 2442.
[223] L. Xue et al., J. Am. Chem. Soc. 139 (6) (2017) 2164.
[224] Z. Xiao et al., Energy Environ. Sci. 13 (9) (2020) 3129.
[225] M. Fiore et al., Chem. Mater. 32 (18) (2020) 7653.
[226] H. Onuma et al., ACS Energy Lett. 5 (9) (2020) 2849.
[227] H. Wang et al., Adv. Energy Mater. 9 (43) (2019) 1902697.
[228] R. Xu et al., Matter 1 (2) (2019) 317.
[229] T. Li et al., Joule 3 (11) (2019) 2647.

Please cite this article in press as: S. Imtiaz et al., Materials Today, (2021), https://doi.org/10.1016/j.mattod.2021.02.008